Crude oil migration in sea-ice: Laboratory studies of constraints on oil mobilization and seasonal evolution

Marc Oggier[a1], Hajo Eicken[a2], Jeremy Wilkinson[b3], Chris Petrich[c4], Megan O'Sadnick[c5]

[a]: International Arctic Research Center, University of Alaska Fairbanks, PO Box 757320, 99775 Fairbanks, USA

[b]: British Antarctic Survey, Cambridgeshire CB3 0ET, Cambridge, UK

[c]: Northern Research Institute (Norut) Narvik, Narvik, Norway

[1] moggier@alaska.edu, corresponding author

[2] heicken@alaska.edu

[3] jpw28@bas.ac.uk

[4] christian.petrich@norut.no

[5] megan@tek.norut.no

1 Abstract

Rising Arctic maritime activities and hydrocarbon development increase the risk of an oil spill in and under Arctic sea-ice. Oil spilled under growing sea ice would be encapsulated within the ice cover. During spring and early summer, such trapped oil would migrate upwards, pervading the ice volume and ultimately pooling at the surface. Current gaps in our understanding of these processes have major implications for spill clean-up efforts and habitat damage assessments. Guided by results from three sets of ice-tank experiments, we have developed a semi-empirical multi-stage oil migration and surfacing model to help predict oil in ice behavior relevant to spill response. According to previous studies, upon under-ice release, oil saturates the ice skeletal layer, remaining largely immobile during the growth season. As intrinsic ice permeability increases above 10^{-11} m^2 with the onset of surface melt, oil migrates rapidly through the full depth of the ice cover, primarily through the secondary pore space. Then, the ever-increasing connectivity between the pores allows the oil to invade the primary pore space. Finally, as the ice deteriorates, oil occupies most of the pore space. Our stratigraphic analysis revealed that granular ice impedes surfacing of oil in cold ice due to the more tortuous pore space. It also showed that the potential for oil movement during the growth season is constrained by the availability of migration pathways from the oil/ice interface to the surface. In contrast to previous findings, our results indicate that if such oil migration pathways are present, significant oil mobilization can occur in cold ice during the growth season. Thus, we tracked upward oil migration through large brine channels in cold ice (T_{ice} <–5 °C) over vertical distances of up to 30 cm, leading to surfacing of oil, within 24 hours after release. During ice melt and deterioration, oil movement is tied to the magnitude of the bulk brine volume fraction and the magnitude of the oil lens reservoir. Development of a predictive oil migration model based on these findings will aid spill response planning, oil detection and damage assessments.

2 Keywords

Sea-ice, crude oil, seasonal cycle,

1 Introduction

Milder ice conditions and economic drivers have resulted in a substantial increase in maritime and hydrocarbon exploration activities in the Arctic (AMAP, 2007; Eguíluz et al., 2016; Smith and Stephenson, 2013). Oil exploration is underway in seasonally ice-covered waters of the Siberian and Alaskan Arctic. In the Prudhoe Bay region in Alaska, several offshore production platforms with subsea pipelines are in operation, with additional offshore leases slated for development (Hillcorp, 2015) . While the length of the open-water season has been increasing (Barnhart et al., 2015; Markus et al., 2009), Arctic waters remain ice-covered for much of the winter and spring—a significant hazard for maritime operations. Any increase in human activity in the Arctic marine environment, such as shipping or oil and gas development, increases the danger of accidental oil spills (Wilkinson et al., 2017). The Arctic Council has identified the ability to respond efficiently to oil spills in marine Arctic environments as a key priority (Arctic Council, 2013).

Spill response and clean-up efforts in ice-covered waters require a thorough understanding of crude oil movement within the sea-ice and oil/ice interaction (Fingas and Hollebone, 2003; Wilkinson et al., 2007). Most importantly, key constraints on oil movement in sea-ice need to be identified and assessed quantitatively, in particular the dependence of oil migration rate on oil properties, and ice microstructure and stratigraphy.

Sea-ice is a composite material, with brine trapped within the ice matrix during sea-ice growth. Initially, small ice crystals that are suspended in the upper mixed layer of the ocean form as a result of seawater freezing. The congelation of this frazil ice layer generates granular ice, which consists of small, isometric and randomly oriented grains. Underneath, the prevalence of quiescent conditions fosters the growth of vertically oriented ice crystals, creating columnar ice. The growth front consists of a high-porosity skeletal layer of few mm to cm thickness with fully connected mm- to sub-mm pore space that makes up the bottommost ice (Petrich and Eicken, 2017). Above, brine channels several cm to dm in vertical extent develop as a result of convective overturning and drainage processes (Cole and Shapiro, 1998; Wells et al., 2011). The brine-filled pore space responds to cooling or warming through increases or decreases, respectively, in brine volume fraction. These changes, in turn affect pore microstructure and ice permeability (Petrich and Eicken, 2017).

Previous studies suggest that in the event of an oil spill during the ice-growth season, oil pools in depressions at the ice/water interface and is encapsulated within 12 to 48 hours, with upward percolation limited

to a few centimetres above the oil lens. Subsequent oil movement is restricted to the skeletal layer and large diameter brine channels. Only later in spring, with increased pore volume and interconnectivity, will the oil be mobilized, invading the bulk pore space, eventually pooling at the surface (Fingas and Hollebone, 2003; Martin, 1979; NORCOR, 1975; Wolfe and Hoult, 1974). Small-scale laboratory studies have shown that oil penetrates sea-ice with porosity as low as 10%, with oil accounting for up to 5% of the bulk ice volume in oil saturated ice with porosity >15% (Karlsson et al., 2011). Oil penetration depths range from 0.05 to 0.1 m during the ice-growth season and increase to 0.15-0.30 m in late spring (Petrich et al., 2013). Those finding are comparable to oil behavior observed in experiments in the natural environment (NORCOR, 1975). Small-scale simulations of brine displacement by oil indicate that buoyancy forces due to the oil/brine density difference are sufficient to overcome capillary forces within brine channels, driving oil upward (Maus et al., 2015).

While ice porosity may serve as a proxy variable to assess oil migration in sea-ice, factors such as permeability, oil layer thickness, ice stratigraphy and pore microstructure, and processes such as brine convection and meltwater flushing also play a significant role in oil entrainment and migration (Maus et al., 2013; NORCOR, 1975). To improve our understanding of the processes governing oil-sea-ice interactions and predict oil distribution after a spill, these factors must be considered over the course of an entire growth-melt cycle and the full vertical extent of the ice cover (Dickins, 1992). Here, we present the results of three oil-in-ice laboratory experiments in which the entrainment, distribution, and migration of oil was observed throughout the entire seasonal cycle and at the full ice thickness scale, to our knowledge for the first time since the NORCOR experiment. The three experiments were:

1. The Cold Regions Research and Engineering Laboratory (CRREL) large-scale ice tank facility: The experiment performed aimed at detection of oil-under-ice through remote sensing means (Pegau et al., 2016),
2. A small-scale ice tank facility at University of Alaska Fairbanks (UAF): The mesocosm experiment assessed the impacts of crude oil on ice biota (Collins et al., 2017), and
3. The Hamburgische Schiffbau-Versuchsanstalt (HSVA) large-scale ice tank facility: The experiment aimed at quantitative prediction of oil movement and distribution in sea ice and implications for near surface detectability (Petrich et al., 2018)

While several experiments have been conducted since the early 1970s, the principal interests were to investigate oil movement over a large surface area, and assess both oil detection and clean-up method (Dickins , 2011). Specifically, we focus on the seasonal evolution of sea-ice porosity and permeability, as well as ice texture (columnar, granular), and on how these factors constrain the oil-sea-ice interactions.

In both the CRREL and UAF experiments we released Alaska North Slope (ANS) crude oil under mostly columnar ice ranging between 20 and 80 cm in thickness. At HSVA, Norwegian Troll B oil was released under 20 cm of ice composed of different stratigraphic sequences. Unexpectedly, at CRREL and UAF, oil surfaced less than 24 hours after release under cold ice (T_{ice} <-5 °C). To our knowledge, this was the first time that oil was observed to migrate through the entire depth of a cold ice cover. One aim of the present paper is to explore how ice and oil properties contribute to oil surfacing in cold ice. More broadly, the ice tank experiments allow for the exploration of ice permeability, oil availability and the importance of sea-ice stratigraphy, especially the presence of granular ice, in constraining the upward migration of oil through the ice cover.

Drawing on the quantitative measurements of oil fluxes into the ice matrix, we describe timing and behavior of oil surfacing with a multi-stage model, which may help to develop a simple oil distribution model to inform spill response and support assessments of habitat damage and impacts on sea-ice biota.

2 Methods

2.1 Experiment set-up

Three sets of oil-in-ice experiments (see Table 1) were completed between 2014 and 2015 in different ice tanks, to test different combinations of oil volume released below ice of different thickness, referred to as “treatments” below. Ice was grown up to 0.3 m thick in a small tank (0.6 m wide, 0.6 m long, 1 m deep) at the Geophysical Institute, University of Alaska Fairbanks (UAF; Collins et al., 2017) in 2014 and 2015, each over a 1-month period . At the Geophysical Research Facility of the Cold Regions Research and Engineering Laboratory (CRREL), Hanover, USA, ice reached a thickness of 0.8 m in a large basin (37 m long, 9 m wide, and 2.6 m deep; (Pegau et al., 2016), mimicking a full seasonal cycle with ice growth, melt and decay over 4 months. In the Arctic Environmental Test Basin (30 m long, 6 m wide, 1.2 m deep) of the Hamburgische Schiffbau-Versuchsanstalt (HSVA), Hamburg, Germany, ice reached a thickness of 0.3 m, simulating conditions corresponding to the end of

the ice-growth season and onset of melt over a 3-week period. Alaska North Slope crude oil was used at UAF and CRREL, and Norwegian oil Troll B was used at HSVA (Petrich et al., 2018).

Treatment parameters, naming conventions, oil origin, under-ice oil lens thickness (h_{oil}), ice thickness ($h_{i, oil}$) and ice type are summarized in Table 1. In the following, treatments with $h_{i, oil}$ <0.3 m and 0.5 m ≤ $h_{i, oil}$ at the time of the injection are referred to as thin and thick ice, respectively. Oil lenses are categorized as thin for h_{oil} <10 mm, medium for 10 ≤ h_{oil} <20 mm and thick for 20 mm ≤ h_{oil}. Dispersed oil refers to a specific treatment at UAF in which a small amount of oil (h_{oil} ≤ 1 mm) was dispersed mechanically into fine droplets during the injection. Treatment names refer to the type of oil used and the thickness of the ice and the oil lens. For example, A18-20c refers to the treatment in which Alaska North Slope oil was released under 18 cm of pure columnar ice and reached a final oil lens thickness of 2 cm. Each treatment included a control treatment without release of oil. We replicated each treatment twice (N=2), except for A29-40c (N=1), A68-90c (N=1), A18-20c (N=4) and A18–20m (N=3).

Table 1 — Key parameters of experiments

Experiment	Treatment	$h_{i, oil}$ (cm)	h_{oil} (mm)	$h_{i, oil}$ category	h_{oil} category	Oil type	Ice type	remarks
UAF	A18-20c	18	20	Thin	Medium	ANS	c	
	A28-5c	28	5	Thin	Thin	ANS	c	
	A28-1c	28	<1	Thin	Dispersed	ANS	c	Oil mechanically dispersed in fine droplets
	A18-20m	18	20	Thin	Medium	ANS	m	
CRREL	A16-10c	16	10	Thin	Thin	ANS	c	
	A26-20c	26	20	Thin	Medium	ANS	c	
	A29-40c	29	40	Thin	Thick	ANS	c	
	A54-60c	54	60	Thick	Thick	ANS	c	
	A68-90c	68	90	Thick	Thick	ANS	c	Oil injection in 3 steps over 1 h
HSVA	B20-30c	20–22	30–40	Thin	Thick	Troll B	c	
	B20-30m	20–22	30–40	Thin	Thick	Troll B	m	

$h_{i, oil}$ ice thickness at oil release; thin: 0 <$h_{i, oil}$ ≤ 0.3 m; thick: 0.5 m ≤ $h_{i,oil}$; medium: 0.3 <$h_{i,oil}$ ≤ 0.5 m
h_{oil} estimated oil lens thickness; thin: 0 <h_{oil} ≤ 1 cm; thick: 2 cm ≤ h_{oil}; medium: 1 <h_{oil} ≤ 2 cm.
ANS Alaska North Slope
c columnar ice
m mixed, granular ice at the surface with columnar ice underneath

In all experiments, columnar sea-ice was grown under quiescent conditions from artificial sea water in a temperature-controlled room. For some treatments at UAF and HSVA, granular sea-ice was initially formed through

mixing of the surface layer either by mechanical agitation (UAF) or by exposing the surface to artificial wind (HSVA). Treatment was stopped once ice formed a 10 cm thick granular layer; subsequent growth was columnar.

At a given ice thickness $h_{i, oil}$, crude oil was injected underneath the ice using a tube inserted through a hole drilled in the ice cover. In the UAF and CRREL experiments, oil was cooled down close to the freezing point of seawater to prevent ice bottom melt. Calculations show that melt caused by the sensible heat stored in oil is negligible, and hence oil was injected near to sea water temperature during the HSVA experiments. During the oil release, care was taken not to introduce air bubbles into the system. After oil release, in most cases ice was allowed to grow below the oil lens for several days before sampling.

Temperature profiles were recorded at each end of the basin for the CRREL and HSVA experiments, using thermistor probes or thermocouple strings frozen into the ice. At UAF, 3 out of the 6 tanks were equipped with a probe. Ice surface temperature, water temperature, and salinity were recorded daily in each tank with a hand-held digital thermometer, or a conductivity probe (6560 Temperature/Conductivity sensors, YSI Incorporated, Yellow Springs, OH, USA).

2.1.1 UAF tests

At UAF, sea-ice was grown in insulated tanks (Figure 1-a) from a 26 ‰ Instant Ocean® aquarium salt solution with the air temperature set to -15 °C. To prevent pressure build-up in the tank, a 15 L bladder filled with antifreeze was installed underwater and connected to an outside collection vessel with a tube. We avoided the creation of convection cells through weak and intermittent mixing with a low-power aquarium pump. Ice sublimation from the top surface was limited by a thin transparent PVC sheet. To fine-tune the growth rate, we used a submersible heater with adjustable output. In treatment A18-20m, a high circulation pump was installed at 10 cm depth to create a thickness equivalent to naturally grown sea-ice, before being shut off to foster columnar growth. At the time of release, oil temperature was between -2 and -1 °C. Each treatment had 3 replicates.

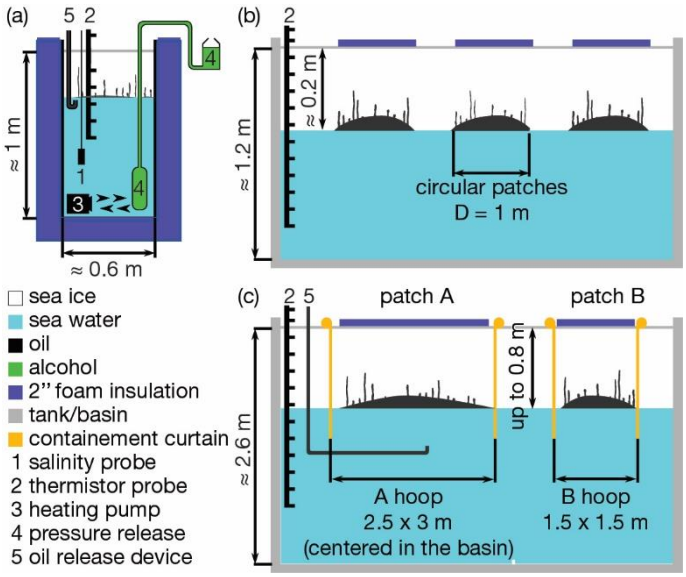

Figure 1 — Schematic of the experiment set-up: (a) at UAF; (b) at HSVA, with circular patches and (c) at CRREL, patches A and B are rectangular. The containment curtains are supported by buoys (yellow).

2.1.2 CRREL tests

At CRREL, 10 oil containment curtains were installed before freeze-up (Figure 1b). Each treatment consisted of 2 replicates: a rectangular patch A (3 m wide, 2.5 m long) positioned at the center of the basin and a smaller square patch B (1.5 m wide) on the side. The control treatment was a 15 m by 3 m area of ice outside of the patches. The cold room was kept at -24 °C during the ice growth period, with ice grown from a 26 g kg^{-1} NaCl solution. We use g kg^{-1} to indicate treatment with NaCl solution and ‰ with artificial sea salt solution. Some treatments with ice thicker than 0.3 m were temporarily covered with insulating foam to inhibit ice growth and create a depression at the ice bottom to decrease the potential of oil spreading outside of the patch. The hole for oil injection was drilled outside of the patch. Oil cooled to 0 °C was injected into the A patch in the morning and into the B patch in the afternoon. Open water was maintained at one end of the basin to release pressure build-up by removing ice when the underwater instrumentation was immersed. At the conclusion of the experiment, air temperature was increased to -2 °C for 14 days, then to 0 °C for the next 8 days and to around 5 °C until the end of the experiment to simulate ice melt and decay under spring conditions. A complete description of the set-up is provided by Pegau et al. (2016). Planning the experiment, based on previous findings, oil was expected to percolate and reach the surface only during this latter melt phase.

2.1.3 HSVA tests

At HSVA, ice was grown from a 30 g kg^{-1} NaCl solution at -12 ˚ C air temperature. In half of the tank, granular ice was grown through forced airflow provided by six WDH-AB10 centrifugal fans. Installation of a wind barrier allowed for quiescent growth of columnar ice in the other half of the tank. Seventeen circular patches of 1 m diameter were created across both ice stratigraphy by temporarily covering the ice surface with foam boards. 7.3±0.6 L of oil were injected into eleven cavities formed at the ice bottom, the remaining patches serving as controls. Air temperature was kept at -12 °C for 3 days to ensure oil encapsulation. Over the next 6 days, air temperature was raised stepwise to -8 °C, -6 °C, -4 °C and -2.5 °C to simulate the onset of melt. We sampled the ice no earlier than 14 hours after initiating each temperature increase to allow time for the ice to adjust to the changed conditions.

2.2 Oil Characteristics

ANS crude oil obtained at the injection point ahead of Alaska Pump Station 1 in 2013 and at a tanker terminal in 2014 on the California Coast was used at UAF and CRREL, respectively. Physical oil properties were characterized for the crude oil used for the CRREL experiment at temperatures of 0 and 20 °C and weatherization degree of 0% evaporation (SL Ross Environmental Research Ltd, Ontario, CA). Dynamic viscosity was measured at a shear rate of 180 s^{-1}. The complete analysis is reported in Pegau et al. (2016). Fresh 2017 Troll B crude oil obtained from the Mongstad terminal was used in the HSVA experiment. Physical properties and composition of a Troll blend were taken from the Troll Blend Assay (Statoil, 2011).

Table 2 — Selected crude oil properties

Oil	Evaporation (Volume %)		Density (g cm^{-3})	Dynamic Viscosity (mPa s)		Interfacial Tension (N m^{-1})		Pour point (°C)
		0 °C	15 °C	0 °C	20 °C	0 °C	20 °C	-
ANS[1]	0.0	0.889	0.877	40	13	0.0270	0.0159	-18 < -40[2]
Troll B	0.0		0.845[3] 0.87[4]	-	6[3]	-	-	-15[5]

[1] analyzed by SL Ross in 2014 (Pegau et al., 2016)
[2] oil was still moving in an elongated jar when tipped over after cooled to -40 °C
[3] Troll blend (Statoil, 2011)
[4]sample measured on-site
[5] there was no apparent oil movement during processing at -15 °C leading us to believe that the pour point of the oil batch was higher.

2.3 Ice sampling

For the UAF and CRREL tests samples were obtained for measurements of bulk salinity, temperature and oil volume fraction, as well as in-ice oil distribution. Ice cores of 5 cm (UAF) and 7.5 cm diameter (CRREL) were recovered with a battery powered barrel ice corer (for details, see Eicken et al., 2014). Temperature was measured by inserting a thermistor probe into holes drilled at 5 cm intervals in an ice core immediately after extraction. Measurement precision and accuracy were in the range of 0.05-0.1 ˚ C and 0.1-0.3 ˚ C, respectively. For salinity, the cores were cut into 2.5 cm (UAF) and 5 cm (CRREL) thick horizontal slices after extraction and transferred to a sealed container for melting at room temperature. Bulk salinity was measured with a YSI 30 conductivity probe (YSI Incorporated, Yellow Springs, OH, USA), with precision and accuracy estimated at 0.05 to 0.1‰ and 0.1 to 0.2‰, respectively. At UAF, oil volume fraction was estimated by measuring the volume of oil and water in a vertical, graduated cylinder, with a precision of 0.5 ml.

Ice stratigraphy and oil distribution were obtained either from an additional core or a vertical slab cut from the ice. Immediately after extraction, cores and slabs were examined visually and photographed to determine ice layering and presence of oil. The slabs were later sliced into horizontal thick sections and vertical thin sections using a bandsaw. Crossed optical polarizers were used to analyze ice microstructure. At UAF, ice was sampled two days before the oil release to establish a baseline, and 10 or 13 days after oil injection to observe the oil distribution. At CRREL, the replicate patch was sampled to capture potential oil percolation throughout the melt period after termination of ice growth.

At HSVA, ice was sampled once its temperature had reached a new equilibrium after each warming phase. Temperature was measured on a 10 x 10 cm square section according to the protocol described above. A larger vertical slab (approximately 10 cm wide, 50 cm long) was extracted for salinity, oil volume content, and microstructure observations. The slab was cooled to -40 °C prior to processing in a laboratory at -15 °C. After removing a 1 cm thick vertical section for photography, the slab was cut into 1 to 2 cm thick horizontal sections throughout its vertical extent. The horizontal sections were later subsampled in 6 or 7 columns of 5 x 5 cm square segments for salinity and oil volume content measurements, with the 1st column centered on the oil lens edge. From melted oil-contaminated samples, the oil was extracted with known volumes of heptane. The oil

concentration in the solvent was then measured using a UV—fluorescence meter TD500TM (Turner Designs Hydrocarbon Instruments, Inc). The instrument was calibrated to crude oil concentrations prior to analysis according to standard procedures (O'Sadnick et al., 2017). Bulk salinity was measured on the aqueous part of the sample.

2.4 Sea-ice Properties Modeling

Sea-ice physical properties were determined from temperature and salinity profiles using semi-empirical equations (Cox and Weeks, 1983; Petrich & Eicken, 2017; Golden et al., 2007). For UAF and HSVA experiments, coincident salinity and temperature data were available. For the CRREL tests, temperature profiles were matched with ice cores that were within 5% of the measured ice thickness (10 % if <3 cores met this criterion). Salinity and temperatures profiles were vertically scaled to an identical ice thickness, averaged and then served to calculate brine volume fraction and permeability profiles.

It is important to point out that the insulating boards, placed on the ice to produce a depression under the ice for oil containment, will impact the thermal profile of the ice. To correct for this we estimated the impact of insulation foam at the ice surface on the temperature field. Based on sonar oil lens thickness measurements we approximated the under-ice depression by a quadratic function. We computed the temperature field by implementing the heat diffusion equation using a finite-element forward model (1 mm grid elements) under the steady-state hypothesis. Temperature at the ice/air interface was fixed to -18 °C during the growth period and -12°C at the oil release, according to ice surface temperature measurements. Thermal conductivity and heat capacity for the overlying ice were calculated from scaled salinity profile data as a function of the brine volume fraction. Sea-ice physical properties were computed from both the model-derived steady-state temperature and salinity fields.

2.5 Tracking Oil Movement

Oil movement was tracked using different approaches at the three experiment sites. At UAF, a digital single lens reflex (DSLR) camera captured the ice surface at regular intervals in one of the tanks for most treatments. At HSVA, three time-lapse cameras Uovision UV785 captured the timing of oil surfacing throughout the experiment with a resolution of 1280x720 pixels. Oil movement at CRREL was observed using a combination

of above-ice time-lapse cameras, underwater cameras and an upward-looking single-beam narrow-band sonar (Aquascat 1000, Aquatech Group, Basingstoke, UK). Three time-lapse cameras (G42NG, Stealth Cam LLC, Grand Prairie, TX, USA; 1280x720 pixels) were installed above the patches for A29-40c, A54-60c and A68-90c to capture the oil surfacing patterns. Images helped determine oil migration rates based on timing of oil surface appearance and known time of oil release. The narrow-beam sonar monitored the thickness of the oil lens under the ice. We recorded the time when oil reached the surface at different locations. Surfacing locations were considered distinct if separated by at least 0.15 m. To quantify oil migration speed, we calculated the vertical migration as the ratio between ice thickness at time of oil release divided by the time required for the oil to surface.

The underwater sensors were mounted on a trolley traveling along the center of the tank bottom. The carriage could be positioned under a specific main patch to observe the ice bottom before, during, and after oil injection. The narrowband single beam unit was equipped with 4 transducers (5, 1, 0.5, 0.3 MHz). The transducers had a beam width of 3.75°, or 0.15 m at the water surface at 2.22 m distance. The return signal of the sonar pulse was sampled into 256 bins of 2.5 or 5 mm. The speed of sound was assumed as 1500 ms^{-1} for the experiment. With this system we estimated the volume of oil infiltrating the ice from the movement of the oil/water interface for the oil treatment without encapsulation (A68-90c). The shape of the underwater cavity was obtained from trolley traverse data, with the ice bottom approximated by a spline curve. The initial location of the ice/water interface and the movement of the oil/water interface was obtained from data recorded at 1 Hz for 3 minutes at the center of the cavity. After averaging the signal over 3 minutes, the position of the oil/water interface (ice/water before oil release) was defined by the signal exceeding a threshold set as the mean plus 5 standard deviations of the noise of the instrument. Oil lens thickness was then equated with the difference between the oil/water interface position and the initial ice/water interface position, assuming a centro-symmetric cavity and a flat oil-water interface.

Large uncertainties (± 2 Lm^{-2}) in the computed volume of oil infiltrating into the ice per unit area were expected because of the 2.5 mm resolution of the AQUAscat transducer. The discretization error in the location of both ice/water and oil/water interface introduced an uncertainty of plus or minus one half the resolution bin size. The uncertainties in oil lens thickness, obtained by subtracting two independently determined distances, is thus of the order of the bin size, and transfers to the volume calculation.

3 Results

Below, we present physical property data to support the validity of laboratory studies relative to field experiments, and to provide context for the analysis of oil movement in sea-ice. Subsequently, we address oil migration throughout a simulated seasonal cycle and mobilization of oil in cold ice, focusing on the spatial distribution of the oil over time as a function of evolving ice properties.

3.1 Ice properties

3.1.1 Stratigraphy

Ice stratigraphy was similar for all three experiments (CRREL, UAF, and HSVA) columnar ice experiments, with a thin layer of granular ice texture up to 3 cm thick at the top and columnar ice below (Table 3). In mixed ice grown at HSVA, approximately 7 cm of granular ice were underlain by a transition layer of 2-3 cm thickness and columnar ice underneath. Stratigraphy and contrast in texture between granular and columnar ice at HSVA are illustrated in Figure 2. Depending on ice growth rate, skeletal layer thickness ranged between 1 and 5 cm.

Table 3—Summary of ice stratigraphy

Thickness (cm)	UAF A-18 columnar	UAF A-28 columnar	UAF A-18 mixed	CRREL columnar	HSVA columnar	HSVA mixed
Granular sea-ice	1 – 2	3	8 – 10	1 – 3	1 – 2	7 – 8
Columnar sea-ice[1]	16	25	12 – 14	16 – 68	21 – 25	12 – 13
Skeletal layer	2 – 4	1 – 2	2 – 5	3 – 5	2 – 5	2 – 5

[1]: including skeletal layer

The columnar ice grew mostly undisturbed at CRREL, except for a layer with small air bubbles at about 40 cm. Ice crystal diameters of up to 7 cm were observed. At UAF, episodic sampling and removal of samples from the ice cover resulted in nucleation of new columnar crystals within a stratigraphic horizon corresponding to the ice bottom at the time of sampling. These discontinuities limited ice crystal growth to a maximum size of 3-4 centimeters. At the time of the oil release, ice crystal size was in the order of 2 cm. At HSVA, columnar ice grew undisturbed, with ice crystal diameters up to 4 cm.

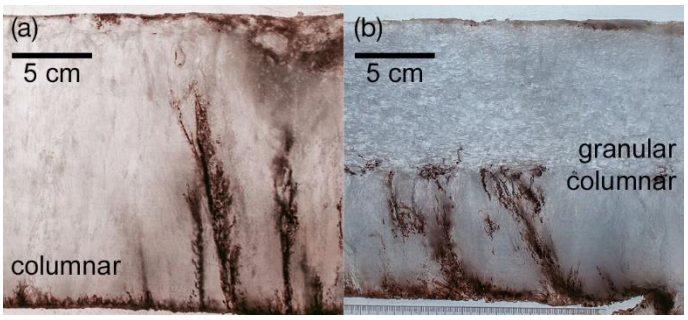

Figure 2 – Vertical thick sections across the entire ice thickness down to the excavated oil lens for columnar ice (a) with and (b) without a granular surface layer at OR+4 of the HSVA experiment. The impact of the granular-columnar transition layer on oil migration patterns is evident. Note the termination and lateral migration of oil, referred to here as fanning, at the granular/columnar ice interface in the right half of the sample

281

282 ### 3.1.2 Salinity

283 For the three experiments, ice salinity profiles were similar to those of ice grown in a natural environment.
284 At the end of the growth phase, profiles exhibited the typical C-shape (Figure 3a), with an average salinity of 8, 5
285 and 9 g kg^{-1} at the top, center and bottom of the ice cover, respectively. The salinity profile in the mixed ice was
286 similar, with a slightly lower ice surface salinity 7 (g kg^{-1}). Differences in ice salinity between multiple cores of one
287 experiment are small (ΔS <1 g kg^{-1}) and fall within the range of natural variability (Gough et al., 2012).

288 ### 3.1.3 Temperature

289 The experiments simulated the seasonal evolution of natural ice, with ice surface temperature (TS) below
290 –10 °C during growth and increasing towards –2 °C during melt. Figure 3b shows the temperature evolution of ice
291 grown to 0.8 m thickness at CRREL. While temperature patterns were similar at UAF and HSVA, because of lower
292 ice thickness (0.2 to 0.3 m, respectively) temperature gradients were steeper. At CRREL, sampling and oil injection
293 resulted in brief warming of the ice surface up to –8 °C (Figure 3b). At UAF, a similar pattern was observed, with
294 ice surface temperatures rising to –6 °C during ice coring prior to oil release. Numerical simulations of the effect
295 of the surface foam insulation indicate that the resulting lateral offset in the ice temperature field inside the patch
296 within which oil was released is small, with isotherms curving minimally upward (Figure 4a).

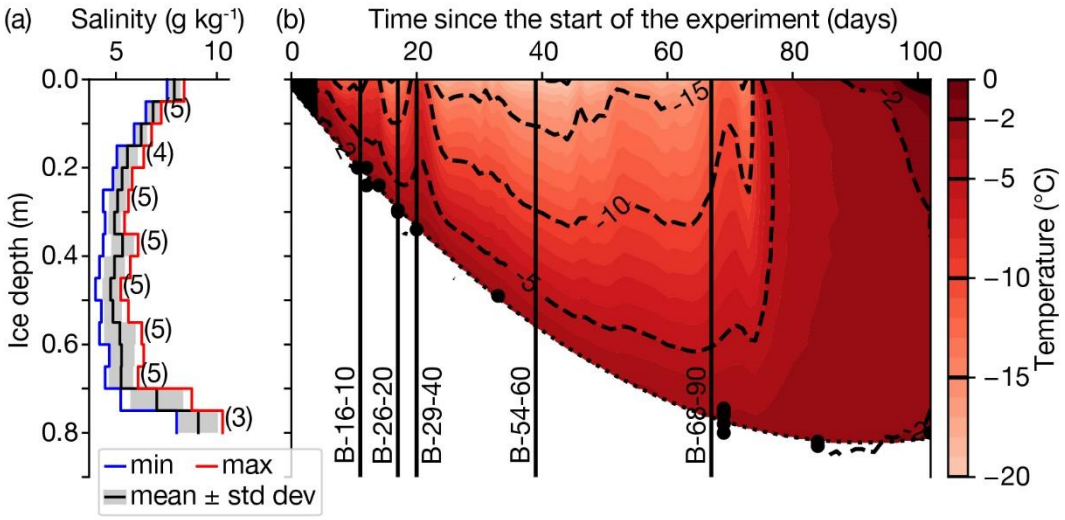

Figure 3 — Salinity profile at the end of the growth season and evolution of ice temperature in clean ice grown at CRREL. (a) Salinity profile at the end of the growth season (t=70 days). Numbers in parentheses specify the number of horizontal sections for salinity measurements. (b) The ice growth curve (dotted line) is the 2nd order best fit of the measured ice thickness (•). Oil injection timing is indicated by vertical lines. During the growth phase (0 - 70 d), ice temperature remained low despite a few brief warming events (D=17-19, 30, 38, 47 d). After 70 days, surface temperature was increased gradually to -2 °C after 70 days, then to 0°C after 84 days and finally around 5 °C to mimic spring decay.

3.1.4 Porosity

We consider the porosity equal to the brine volume fraction in clean ice and the sum of oil and brine volume fraction for oil contaminated ice. In both cases, brine volume fractions are computed from temperature and salinity profiles using the equations of Cox and Weeks (1983) and Leppäranta and Manninen (1988). In the ice above the oil release, porosity was below 5% in cold ice, increasing to 15% in the lower 10 cm closer to the ice/water interface. Treatment A-26-20-c is shown as an example in Figure 4b. After the oil injection, the oil acted as an insulating layer (Figure 4c). Brine volume fraction remained below 5% from the ice surface to 10 cm below the oil lens.

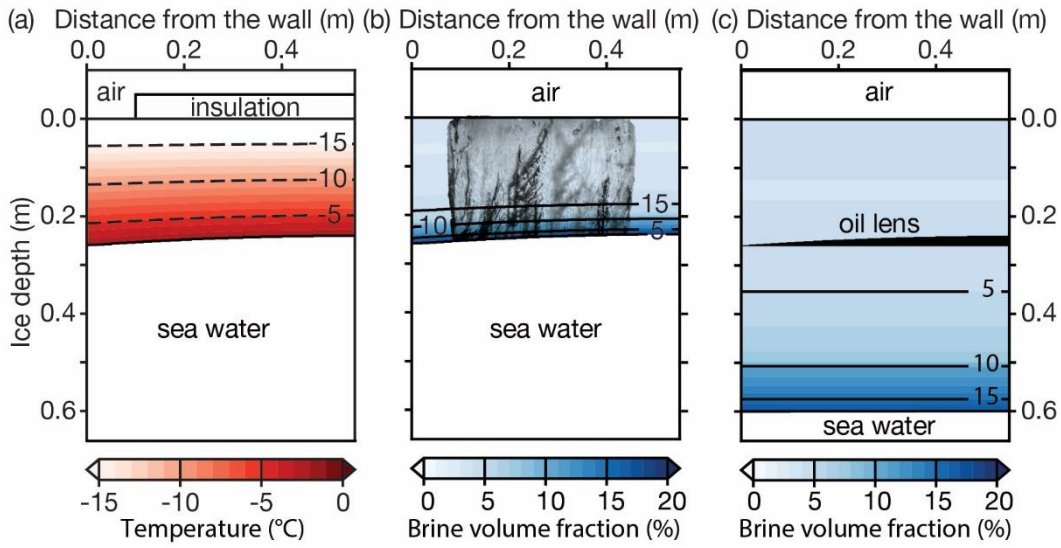

Figure 4 —Simulated temperature field (a), porosity field for A-26-20c at oil release (b), and at the end of the growth season (c). Figure 3b overlays an ice slab (0.45 m wide) at the correct scale that was collected approximately 0.1 m from the wall. Brine channels visible as dark features all contain crude oil.

3.1.5 Permeability

The sea-ice permeability, κ, was computed as a function of brine volume fraction, ϕ, using a hierarchical percolation model valid for columnar ice (Equation 1, Golden et al., 2007).

$$\kappa(\phi) = 3\,\phi^3 10^{-8}\ \text{m}^2 \quad (1)$$

In light of lack of data, but recognizing the limitations of the model, we used the same approach for derivation of granular ice permeabilities. During the ice growth phase, permeability was low throughout the ice cover, with the exception of the lowermost and uppermost layers where higher salinity (and temperature for the ice/water interface) leads to increased porosity (Figure 4b and c).

Figure 5 depicts the evolution of sea-ice permeability from the end of the growth period at the time of oil release (OR) through the end of the melt period 34 days later (OR+34). To compute the 6-hourly porosity, the salinity field was interpolated between coring events and the temperature field was averaged for each 6-hour period. Within 3 days following onset of melt (OR+7 to OR+10), sea-ice permeability increased rapidly (from $\kappa < 10^{-11}$ m^2 in the ice interior) by up to two orders of magnitude as the ice responded to the warming. After OR+15, ice temperature increased at a slower rate trending towards the asymptotic value of sea-ice melting point

(approximately –0.3 °C at for 5 g kg^{-1} seawater). The subsequent changes in permeability were mostly due to brine movement and sea-ice desalination, including the low permeability surface layer at the end of the experiment.

Total porosity data for CRREL and UAF is based on bulk ice salinity measurements in the clean ice treatments. We assume similar pore space evolution in terms of bulk porosity for both clean ice and oiled ice treatment, but have to recognize that replacement of brine by oil will affect pore space evolution. For HSVA, the total porosity is derived from the sum of the brine-filled pore space obtained from salinity measurements and oil-filled pore space computed from oil concentration. Uncertainties are introduced by brine and oil drainage and loss during sample collection.

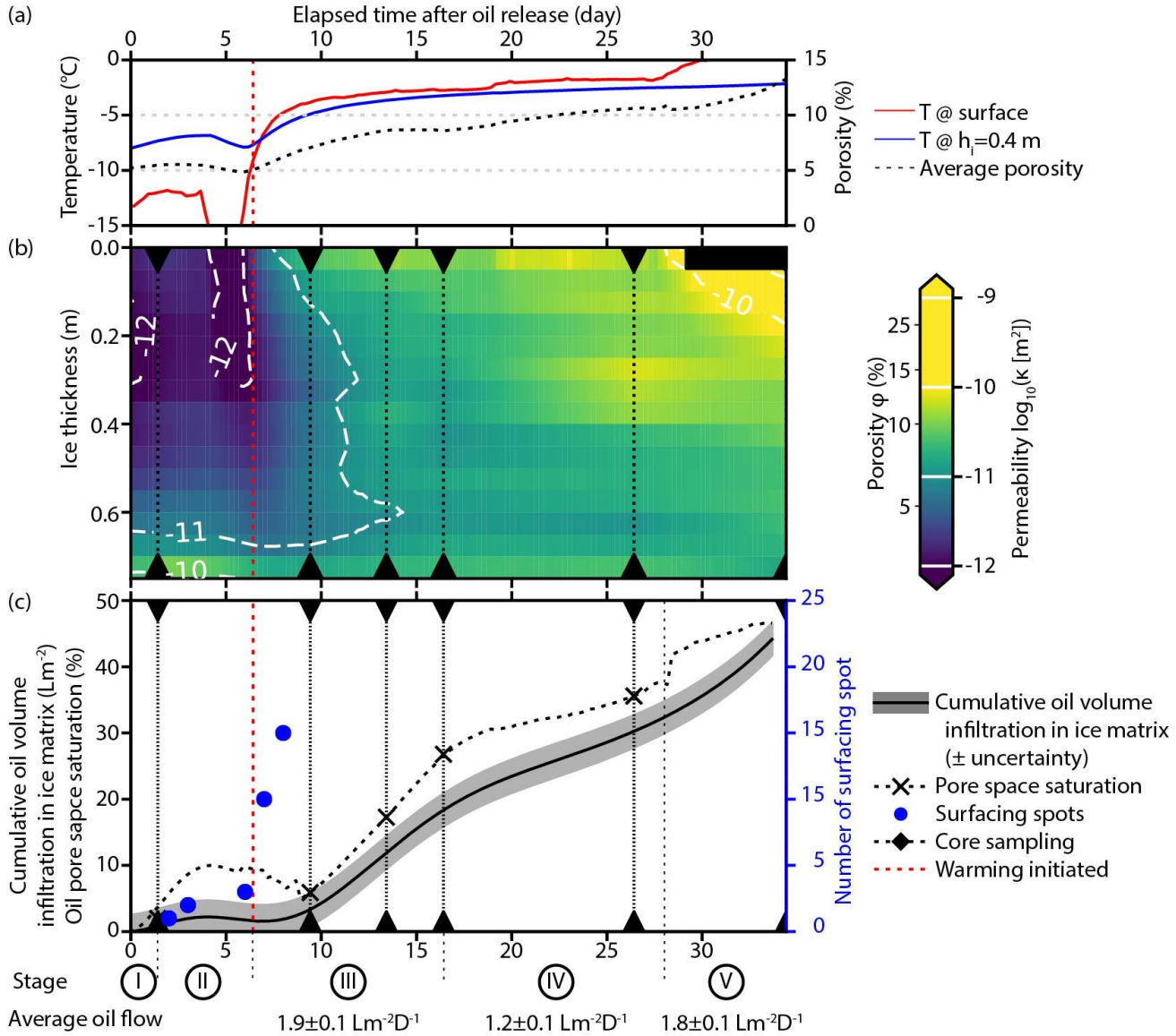

Figure 5 –Temperature, permeability and oil percolation for A68-90c from the oil release at the end of the growth period through the end of the melt season (middle panel). Warming was initiated at OR+7 (red dotted line). (a) Temperature and porosity at selected depths. (b) The permeability field was computed from interpolated salinity, collected during coring events (𝑰) and temperature measurements. Panel (c) illustrates oil movement with the cumulative volume of oil infiltrating the ice matrix (Vo), the pore space saturation as well as the number of distinct surfacing spots. Circled roman numeral indicates the different stages.

326

327 3.2 Oil movement

328 3.2.1 Oil mobilization and movement throughout a simulated seasonal cycle

329 In the CRREL experiments, treatment A68-90c consisted of oil injection at the end of the ice growth period
330 with no subsequent encapsulation of the oil lens. Hence, we were able to accurately track the position of the
331 oil/water interface using hydroacoustic techniques from the point of oil release (OR) until the end of the experiment.
332 This circumstance allowed for the determination of oil fluxes into the ice cover, in conjunction with oil content
333 measurements from ice cores and analysis of oil distribution patterns from thick section stratigraphy, an approach
334 that to our knowledge has not been pursued in previous studies. The bulk infiltration of oil into the ice cover derived
335 from these measurements over time is summarized in the bottom panel of Figure 5. Also shown are the evolution
336 of ice permeability as a key parameter to constrain upward oil percolation, the pore space saturation, and the
337 number of spots where oil appeared at the ice surface by percolating upward through pores and in particular brine
338 channels (Figure 4b , 6, 7). A time series of the latter serves as a proxy for oil percolation through the full depth of
339 the ice sheet. The pore space saturation by oil is defined as the ratio of oil volume within the pore space relative
340 to the total volume of the pore space available for the oil. Postulating that brine, and by extension oil, movement
341 is strongly limited below a porosity of 5% (Karlsson et al., 2011; Pringle et al., 2009), we computed the total volume
342 of relevant pore space as the cumulative sum starting at the bottom of each section in which the brine volume
343 fraction exceeds 5%. Based on this data we recognize five distinct stages of oil entrainment, mobilization, and
344 movement in Figure 5c.

345 Stage I: In the first stage, directly after oil release (OR to OR+2), a small amount of oil quickly penetrated
346 into the ice (V_{oil} = 2±2 Lm^{-2}). This oil infiltration was essentially limited to the skeletal layer, as the open and
347 connected pore space facilitates the displacement of the resident brine. In addition, a small fraction of the oil was
348 detected at the surface starting at OR+2 (Figure 6, location ②).

Stage II: During the second stage, the upward migration of the oil/water interface remained below the detection threshold through the end of the growth period (OR+7), indicating that trapped oil remained immobile. Nevertheless, despite low ice cover permeability ($\kappa < 10^{-11}$ m^2) we observed oil surfacing through at least 3 discrete brine channels (Figure 6, ②, ③ and ⑥). Similar observations were made for A-29-40c and A-54-60c.

Stage III: The third stage begins with the start of the simulated melt season (OR+8 to OR+17). Initially a small amount of oil moved upward, before the flow accelerated and the rate increased up to an average of Q_{oil} =1.9±0.1 Lm^{-2}day^{-1} calculated from OR+10 to OR+17. With the associated increase in permeability, oil appeared in numerous, apparently random locations at the ice surface (Figure 6, ⑦). Freshwater, originating from the defrost cycle of the cooling panels in the ceiling above the ice surface, built up in an ice mound in some areas of the main patch (Figure 6), thus potentially reducing the amount of oil observed at the surface. The number of surfacing spots increased from 7 at OR+7 to more than 30 at OR+9. At the same time surface temperature increased from –9 °C to –4 °C. After OR+10, horizontal spreading of the oil near and at the surface made it impossible to detect new surfacing spots or distinguish new from old spots.

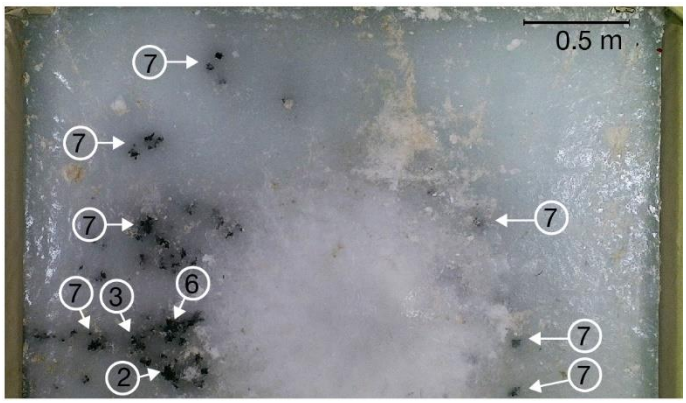

Figure 6 —Spatial distribution and timing of oil surfacing for A-64-90c. Numbers indicate the number of days between oil release and oil surfacing at a specific location. Arrows indicate the approximate location where the brine channels, through which oil migrated, emerged at the ice surface. At oil release, ice surface temperature was T_S = –14°C and reached T_S = –9 °C at OR+7. With the warming of the air (OR+6), oil movement accelerated. The whitish circular patch at the bottom center is refrozen freshwater water dripping from the ceiling-mounted cooling panels during defrost cycles.

Stage IV: In the fourth stage from OR+18 to OR+27, as the ice became isothermal with air temperature held at 0 °C, we observed a decrease in the flow rate down to an average of 1.2 ±0.1 Lm^{-2}day^{-1} from OR+17 to

OR+27. A decrease of similar magnitude is measured for the daily average change in porosity from +1.4 % day^{-1} during stage III to +0.9 %day^{-1} for stage IV. The change in the flow rate coincided with oil saturation having increased to 30%, though correlation between both quantities is difficult to establish due to the disproportionately large increase of porosity as the ice warm above -2 °C.

Stage V: Finally, we recognize a fifth stage commencing as air temperature increased at the end of the experiment (OR+28). Oil flow increased to an average of 1.8 $Lm^{-2}day^{-1}$ from OR+27 to the end of the experiment at OR+34. In the decaying ice, oil pooled at the surface (additional material, Figure 12) , and invaded intra- and intergranular pore space (Pegau et al., 2016, additional material Figure 13).

The HSVA experiment focused on changes during melt onset and yielded similar findings for stages 1 to 3. Overall, pore space saturation values rose dramatically once minimum permeability had increased above 10^{-11} m^2 in both columnar and mixed ice (Figure 7). The evolution of oil volume fraction as a function of depth, averaged across 5 cm sections, is a good proxy for oil migration patterns (Figure 7). After oil release during the growth period (OR), oil movement was limited to the lowermost 5 cm section (stage 1 and 2). Figure 2a shows the vertical movement of oil in discrete brine channels at OR+4. Following the onset of the warming at OR+4, more oil from the lens infiltrated the bottom 5 cm of the ice (beginning of stage 3). At OR+6, the increase in temperature, followed by minimum permeability rising above 10^{-11} m^2, allowed the oil to flow upward and migrate through the ice. At the end of the experiment, significant differences in oil intake were measured between mixed ice, $V_{oil,m}$= 2.6±0.03 Lm^{-2}, and columnar ice, $V_{oil,c}$=1.4±0.02 Lm^{-2}.

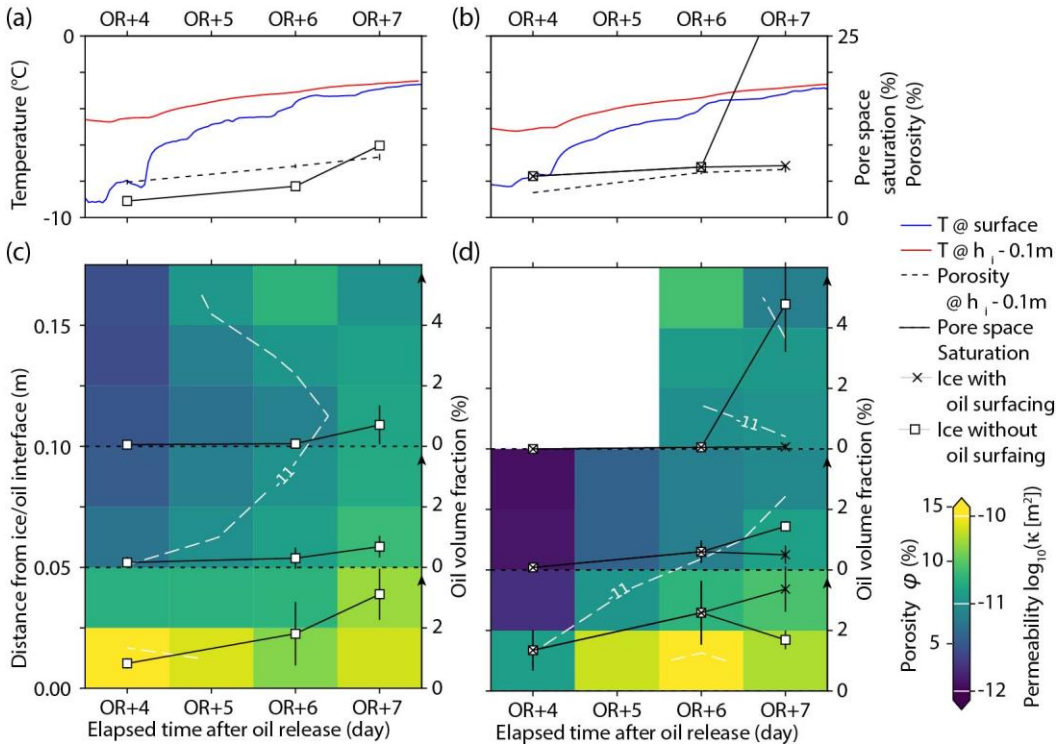

Figure 7 – Evolution of temperature and porosity (a, b) and permeability and oil volume fraction (c, d) as a function of depth and time for (a, c) pure columnar sea-ice and (b, d) mixed sea-ice during the HSVA experiment after the oil release OR. Oil volume fraction was averaged over the skeletal layer (0-2.5 cm), the columnar ice (2.5-10 cm) and the surface layer (either columnar or granular, 10-17.5 cm). Permeability, in the background, was computed from salinity and temperature profiles discretized on a 2.5 cm grid.

3.2.2 Oil surfacing in cold ice

ANS crude oil surfaced within 2 to 4 days after the oil release in cold ice (T_{ice} <–5°C). Oil surfacing in cold ice had almost never been reported previously (Glaeser and Vance, n.d.; Karlsson, 2009; NORCOR, 1975; Otsuka et al., 2004; Petrich et al., 2013; Wolfe and Hoult, 1974) . The observed surfacing in thin (<0.2 m thick) ice was attributed to the light crude oil used, originating from the Gulf of Mexico (Dickins et al., 2005). Initial oil movement (stage I) was limited to discrete brine channels connecting the oil lens to the ice surface (Figure 6). We first observed this behavior during the growth period in the thin ice experiment at UAF (A18-20c). Oil surfacing was limited to medium and thicker oil lens thickness (h_{oil}> 1 cm, A18-20c), and absent for thinner oil lenses (A16-10c, A18-5c, A18-1c). During the CRREL experiment – only thick and medium oil lens thickness, oil reached the surface within 3 days after each oil release for ice thickness ranging from 20 to 68 cm. As at UAF, no surfacing was observed for a thinner oil lens (A16-10c). At HSVA, oil movement was slower overall than in the two other experiments. Use of Troll B, rather than ANS crude oil, may explain the slower pace in thin ice, despite the thicker

oil lens (B20-30c, B20-30m). While oil surfaced at a single location in mixed ice at OR+1, overall the oil reached the surface in different replicates at OR+4 in both columnar and mixed ice.

During the ice growth phase, we observed crude oil within the skeletal layer and in the brine channel system (Figure 7, Figure 8a). Overall, oil volume fraction decreased with distance from the oil/ice interface (Figure 7). Penetration depths ranged from a few centimeters above the skeletal layer to the full depth of the ice cover (A-26-20c and A-23-20c). When in direct contact with oil, the space between the ice lamellae of the skeletal layer was homogeneously invaded (Figure 8a). Above the skeletal layer, oil movement appeared to be limited to brine channels, ranging from 2 to 5 mm in diameter (Figure 2, Figure 8b), in particular those closer to the edge of the oil lens (e.g., Figure 2). Some fanning, with oil entering smaller tributary channels is visible in Figure 2a, but most of the feeder channels remained free of oil. The horizontal spacing between channels is roughly 10 cm when examining vertical thick sections, with fewer than half filled with oil before the end of the growth period.

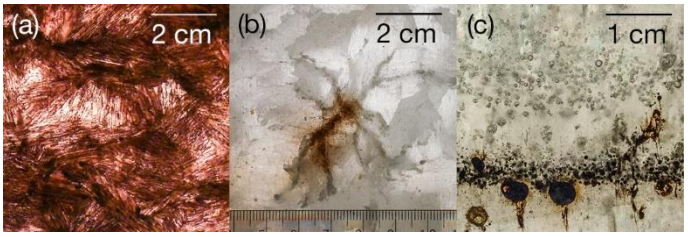

Figure 8 — Horizontal thick sections showing oil distribution: (a) in the skeletal layer, 1 cm above oil/water interface (A-20-30c); (b) in a brine channel with fanning into feeder channels, approximately 10 cm above oil/water interface (A-20-30c); (c) vertical thin section of the dispersed oil treatment (A-28-1c) (scale bar in cm).

In the treatments shown in Figure 9, we differentiated 4 subsets characterized by the thickness of the oil lens, oil lens thickness, and the ice developmental stage towards the end of the growth season using a Tukey test with a significance level of 0.05.

First, in thin oil treatments ($h_{i,\,oil} < 1.5$ cm), oil movement was restricted to the bottommost layer with little penetration of brine channels (Figure 9, A-28-5c and A-28-1c). In the dispersed oil treatment (A-28-1c), oil coalesced in droplets underneath the ice/water interface. Only thin droplets were entrained within 1 centimeter of the skeletal layer, and on rare occasions oil moved further up into the pore space.

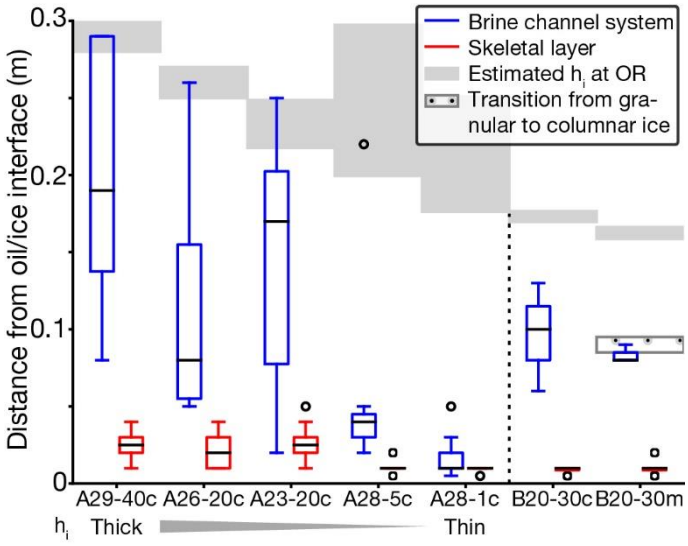

Figure 9 — Oil penetration depth measured upwards from the ice/oil interface for saturated brine channels (blue) and skeletal layer (red), with h_i the ice thickness. All depths were measured at the end of the ice growth period, except for A29-40c, recorded a day after the onset of melt but included here as ice porosity was still below 5 %. The box shows the median with the first and third quartiles and whiskers set at 1.5 interquartile range*. Small, singular amounts of oil ("outliers") are marked (○). The vertical dotted line separates treatments with different types of oil. Note treatments with Troll B oil had thick oil lenses (B20-30c/m).*

Second, within the medium and thick oil lens treatments ($h_{i,\,oil}$> 1.5 cm), oil was entrained through the full depth of the skeletal layer estimated at 3 cm (Table 3), and oil movement in the brine channels was mostly limited to the lower part of the ice, except for three channels filled up to the ice surface. A26-20c and A23-20c are representative of a medium ANS oil lens thickness at the end of the growth period (stage 2).

Third, treatments with Troll B oil (B20-30c, B20-30m), despite a thicker oil lens than for A26-20c and A23-20c, display moderate oil movement, with an average penetration depth of half the ice thickness. In contrast with ANS crude oil, Troll B oil did not penetrate through the full ice cover thickness and the penetration depth is homogeneous, independent of the brine channels. The skeletal layer, thinner for the HSVA experiment, appears saturated in oil.

Fourth, oil penetration into the skeletal layer for A-29-40c was similar to A-26-20c and A-23-20c. However, oil moved deeper into brine channels, with the upper range of the box plot matching the location of the ice surface. A-29-40c was sampled just after the onset of melt during the CRREL experiment. In the third stage of oil migration,

the increase of porosity and associated widening of brine channels allow the oil to reach the surface through a larger number of channels.

The vertical migration rate of oil in ice shows no clear correlation with ice lens thickness, ($h_{i,\,oil}$), ratio of oil/ice thickness, bulk or effective bulk permeability (Figure 10). Vertical migration rates tended to be fastest in thin and columnar ice, although values varied significantly between treatments (Figure 10a, $h_{i,\,oil} < 20$ cm). In treatments with thick oil lenses ($h_{oil} > 4$ cm), faster oil migration rates were observed with increasing columnar ice and oil lens thickness (Figure 10a, A54-60c and A68-90c, dashed circle). Oil surfaced fastest for A29-40c, a treatment with thin ice and thick oil lens. The two replicates for these three treatments were part of the same set of experiments at CRREL. Due to the small sample size and lack of cross control, interpretation should be subject to caution. Under similar ice and oil thickness conditions, the oil surfaced faster in columnar than mixed ice stratigraphy, except in one of the 11 B20-30m replicates in which Troll B surfaced earlier in a single channel in mixed stratigraphy (Figure 10a, compare B20-30m/red • to B20-30c/red x).

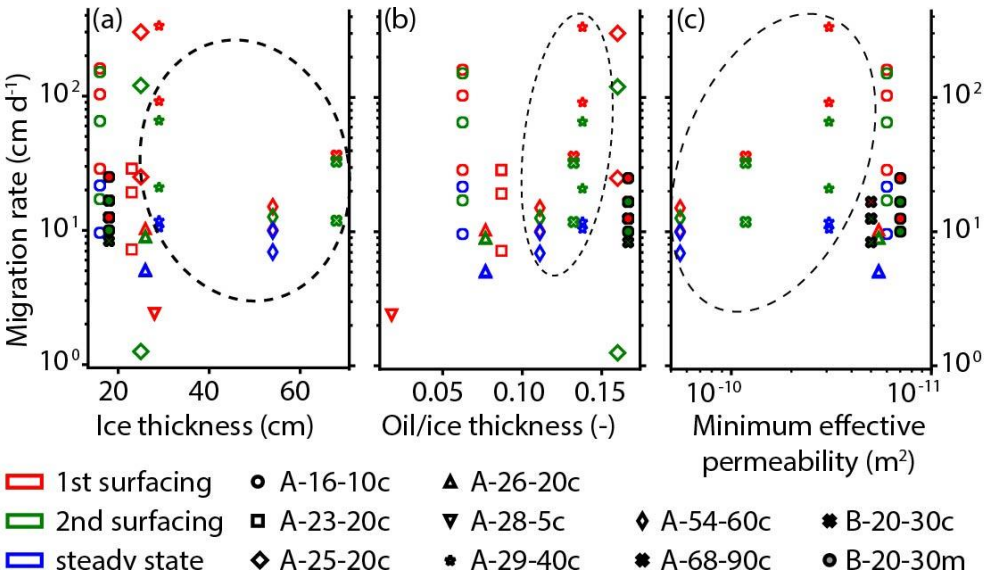

Figure 10 — Vertical oil migration (cm d^{-1}) rate as function of (a) ice thickness, (b) ratio of oil to ice thickness, and (c) permeability. Migration rate has been computed from the time elapsed between oil release, and the detection of the 1st surfacing location (red), detection of the 2nd surfacing location at least 0.2 m away from the first one (green), and once oil flow stopped and the surface pools remained in position (blue). The dashed ellipse encompasses the treatments with thick oil and ice lenses.

3.2.3 Ice stratigraphy and oil movement

We observed striking differences in oil behavior between different sea-ice stratigraphic units at HSVA (Figure 2). During the ice growth phase, upward oil movement was limited to brine channels in columnar ice. In mixed ice, such vertical percolation terminated at the interface between columnar and overlying granular ice. Oil penetration depths were limited to about 9 cm in mixed ice (Figure 9, B20-30m), corresponding to the position of the columnar-granular ice transition layer. In pure columnar ice, penetration depths ranged from 6 to 13 cm (Figure 9, B20-30c). Analysis of bulk oil content largely confirms this pattern (see Figure 7). Those results are consistent with the mixed ice treatment at UAF (A-18-20m): oil surfacing occurs only once in one of the three replicate tanks through the granular ice, though oil movement was extensive through the columnar ice underneath.

During the early melt phase, we observed similar patterns of oil movement in the columnar ice in vertical thick sections independent of the stratigraphy (cf. additional online material Figure 14-21). Large standard deviations are to be expected in the oil concentration measurements due to the heterogeneity of the oil migration and relatively small column area (5 x 5 cm^2).

Before the onset of melt, oil was concentrated within the skeletal layer with an average oil concentration of 1.09±0.42 % (0 – 2.5 cm above the oil/ice interface). We observed some oil migration in distinct brine channels in the lower part of the columnar ice, where oil concentration reached 0.12±0.13 % (2.5 - 10 cm above the oil/ice interface; Figure 7c/d, OR+4). Small amounts of oil migrated into the subsurface layer with a concentration of 0.06±0.12% (10-15 cm above the oil/ice interface) in columnar ice treatments (Figure 7c, OR+4), but remained below detection level in granular ice (Figure 7d, OR+4).

As the ice warmed up at OR+5/6 (Figure 7), oil mobilized in the lower half of the ice and started invading feeder channels along the main channels (cf. additional online material Figure 14-19). On average, the oil concentration increased twofold both in the skeletal layer (V_f = 2.20±1.05 %) and in the lower columnar ice (V_f = 0.45±0.36 %), independently of the stratigraphy. In the columnar stratigraphy, oil reached the surface in discrete brine channels, with an oil concentration of 0.09±0.09 % in the subsurface layer. In mixed stratigraphy, observations of lateral spreading of the oil below the columnar to granular transition matched the higher oil volume fraction of 0.45±0.37 % in the lower columnar ice relative to 0.19±0.22 % in columnar stratigraphy. In the granular ice, oil concentration remained low (V_f = 0.05±0.08 %), despite a visually highly impacted ice matrix (cf. additional

online material Figure 19). An observation made earlier by Martin (1979) small amounts of oil produced very dark cores.

By the end of the experiment (OR+7), increased permeability throughout the ice column corresponded to an increase in oil volume fraction in both columnar ($V_{f,oil}$ = 0.9 ±0.6 %) and mixed stratigraphy ($V_{f,oil}$ = 1.5±1.2 %). Oil concentration increased in the skeletal layer to as much as 3.0±0.9 % and up to 0.7±0.6 % in the lower part of columnar ice (2.5 – 10 cm) We counted a surfacing spot density of 170 m^{-2} in columnar ice and one tenth of that in mixed ice (Supplemental material Figure 24, 22). Vertical sections revealed not only extensive horizontal oil spreading (Supplemental material Figure 21), but also very heterogeneous distribution in granular ice. These observations correlate with the oil concentration measurements. In the subsurface layer, the oil volume fraction was on average higher in granular ice at 1.6±2.4%, versus 0.2±0.6 % in columnar ice. However, in some samples where the oil did not surface, oil concentration in the granular ice was below detection levels. In samples where the oil did surface, concentrations of up to 4.8±0.6 % were observed.

4 Discussion

4.1 Comparison of laboratory-grown with natural sea-ice

Bulk salinity and temperature profiles of the columnar ice grown during the three experiments are representative of natural sea-ice growth under quiescent conditions, such as landfast ice, with the characteristic C-shape curve with higher salinity at both interfaces, and linear profiles during the growth season (Petrich and Eicken, 2017). The typical approach used to grow artificial sea-ice in small tanks, as at UAF, or large basins, as at CRREL, generates only a thin layer of granular ice (<5 cm) at the surface – much thinner than what is typically observed in natural environments (Galley et al., 2015; Weeks, 2010; Zubov, 1963). A thicker granular ice layer can only be obtained through forced mixing of the upper water column resulting in formation of frazil ice during onset of freezing. At HSVA, fans simulating wind mixing over leads (Bauer and Martin, 1983), resulted in formation of frazil ice that consolidated into a 7 cm granular ice layer. Since this approach fails in small tanks lacking sufficient fetch, UAF experiments employed a high circulation pump installed at depth to attain the desired granular ice thickness. Thick and thin sections confirm that both columnar and granular ice in all treatments was representative

of natural ice textures. Findings from all three experiments indicate that the timing of oil surfacing is strongly affected by the presence of granular ice.

During the CRREL experiment, the presence of the curtains may have affected brine movement, in particular close to the curtain. In contrast, ice grew entirely undisturbed at HSVA until a few days before oil injection. Although, this may have affected surfacing behavior, the observed presence of brine channels longer than 0.5 m (Cole and Shapiro, 1998), and the lack of vertical sections excavated at the end of the growth season at CRREL make interpretation difficult. A 5-stage conceptual model of oil mobilization and movement through a full seasonal cycle.

Maximum ice thicknesses of 0.3 and 0.8 m are limited to 1/3 of the tank or basin depth, to avoid any disturbance in the ice growth as salinity increases in the water underneath. Treatments in thin ice are representative of either the early growth season, or ice forming on exposed open water among broken ice or fragmented landfast ice. Treatments in thicker ice are representative of mid-winter to late winter condition, as currently found in the Alaska Arctic, typically in Utqiaġvik (Eicken., 2016).

4.2 A 5-stage conceptual model of oil mobilization and movement through a full seasonal cycle

Combined observations from all three experiments show consistent stages of oil mobilization and movement through sea-ice during a simulated full seasonal cycle. This behavior can be understood in terms of sea-ice permeability evolution (Figure 5), ice stratigraphy (Figure 7) and type of oil (Figure 9). Our analysis is partly limited by ice thickness, with 9 out of 11 treatments attaining thicknesses of <0.3 m at the time of oil release. The large scatter of oil migration rates in thin ice (Figure 10) is linked to the comparatively large number of thin ice treatments and replicates derived from the UAF experiment: despite the consistency of ice thickness, variability between tanks in surface temperatures as well as growth and melt conditions affected ice microstructure and subsequently oil movement. In contrast, the highly consistent observations from medium and thick ice treatments at CRREL and the different HSVA replicates are explained by consistent ice growth and decay conditions throughout the tanks.

Our simple model of upward oil movement in sea-ice considers oil buoyancy in water – depending on both oil lens thickness and oil density – as the primary driving force. Capillary pressure in the pore space, which depends on oil interfacial tension and pore space curvature, hinders oil percolation at the microstructural scale (Maus et al., 2015). In addition, we neglected that the creation of a new surface between oil and ice as oil displaces brine will restrain oil migration. Hence, we further assume that the oil is only able to move through connected pores whose size exceeds a critical diameter. Furthermore, for the oil to reach the surface, a pathway – defined as a succession of connected pores – must connect the oil lens to the ice surface. As oil invades a pristine pore, a corresponding volume of brine is displaced. The expelled brine may trigger larger-scale brine movement in the connected pore space, or induce microstructural changes to maintain local thermodynamic equilibrium.

Viewed broadly, our observations of oil movement throughout a simulated seasonal cycle support the model of oil migration in sea-ice as described previously: Oil spilled under ice is quickly encapsulated during the ice growth season, and subsequently mobilized during melt, eventually moving upward as the ice warms and decays (Karlsson et al., 2011; Martin, 1979). The detailed data collected here, in particular oil volume flux measurements (likely a first at this resolution), and calculation of ice permeability and oil distribution in relation to ice and pore microstructure, allow us to develop a more refined conceptual model of oil movement in ice. Specifically, we recognize 5 distinct stages discussed in more depth below in relation to physical and microstructural/stratigraphic constraints (Figure 5 and 11). Table 4 summarizes the impacted pore space, the potential for oil movement and the constraining factors we identified for each stage.

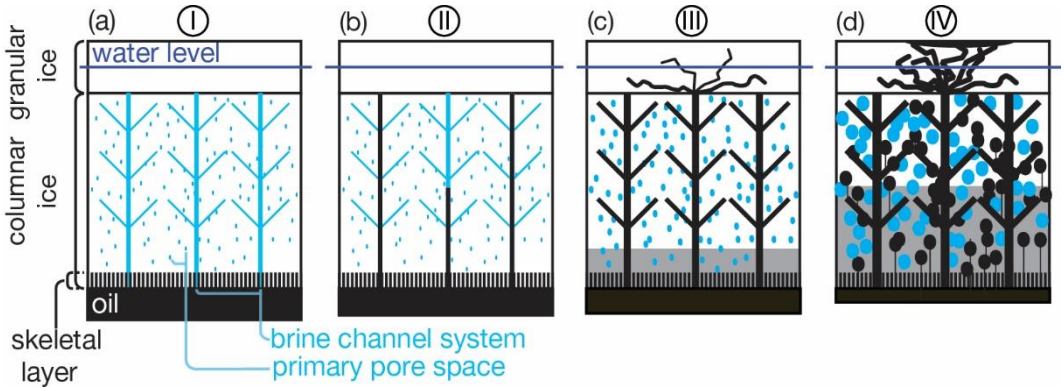

Figure 11 – Cartoon of the 4 first stages of upward oil migration: (a) Initial entrainment in the skeletal layer; (b) Localized upward migration in large channels; (c) Mobilization and incipient bulk infiltration; (d) Steady state infiltration. The fifth stage of disintegration of the sea-ice cover is not pictured. Note the decrease in oil lens thickness as the oil migrates upward into the ice matrix. Circled roman numeral indicates the different stage

Table 4 – Summary of impacted pore space and potential oil intake for each stage

Stage	Oil intake	Oil penetration	Pore space saturation	Impacted pore space	Constraining factors for oil migration	Stage in seasonal cycle
I	< 2-4 Lm^{-2}	2 – 5 cm	< 5 %	Skeletal layer	Low vertical permeability, κ_v	Winter growth
II	0.5 – 1.0 Lm^{-2}	Columnar ice thickness	< 5 %	Large brine channels	Brine channel diameter Existence of migration path Low permeability $\kappa_v < 10^{-11}$ m^2	Winter growth
III	2.5 $Lm^{-2}day^{-1}$	Full ice cover	5 – 30 %	Brine channels and feeders; Connected secondary pore space	Connected pore space Low permeability 10^{-11} $m^2 < \kappa$	Onset of melt
IV	30 Lm^{-3}	Full ice cover	> 30 %	All available pore space	Force balance between oil in lens, ice or at the surface	Melt season
V	Entire oil volume, migration to water/ice surface	Full ice cover	30 – 100 %	All available pore space	Available pore space	Late melt season

4.2.1 Stage 1: Initial entrainment and encapsulation

Shortly after the oil release, within three days at most based on analysis of ice slabs, oil invades the skeletal layer just above the ice-oil interface as a key aspect of initial oil entrainment. The open and highly connected pore space of the skeletal layer (Petrich and Eicken, 2017) allows oil to displace resident brine (Figure 8a). Horizontal permeability in this bottom-most ice layer, one to two orders of magnitude higher than in the vertical direction (Freitag, 1999) remains large enough for the brine to circulate, likely to be expelled at the ice/water interface, away from the oil lens. Within the first day, the average (and maximum) volume of oil invading the ice of 1.5 (3.5) Lm^{-2} was easily absorbed by the bottommost 1.5 (3.5) cm of the ice cover, assuming an average porosity of 30 % and a pore space saturation of 30% (i.e., an oil volume fraction of 9%). The penetration depth values are in agreement with simulations for natural sea-ice pore space (Maus et al., 2013). The volume of oil absorbed in the skeletal layer falls within the estimation of 0 to 4 L by Petrich et al. (2013) for an oil spill in winter.

The lack of further movement of the oil/water interface beginning at OR+3 (Figure 5) until the end of the growth season indicates that an equilibrium had been reached. Oil stops migrating into the ice and the initial phase of oil entrainment ends.

In conjunction with oil entering the skeletal layer, with continued ice growth the oil lens was gradually encapsulated by ice encroaching from the edges of the under-ice depression. At CRREL, full encapsulation of the oil lens occurred after OR+2 and OR+3, for thin ice treatments A26-20c and A29-40c, respectively. In thick ice (A68-90c) ice encroachment was too slow to seal off the oil lens by the start of the melt period (OR+6). At HSVA, ice encroachment started before OR+4, fully encapsulating the oil lens (30 mm thick) by OR+6. Previous studies have reported full encapsulation of a 10mm thick oil lens within 24 to 48 hours under 160 cm of ice (Buist and Dickins, 1983; Dickins and DF Dickins Associates LLC, 2011). For droplets and smaller oil lenses (<1L), encapsulation in less than 12 hours has been observed (Petrich and Arnsten, 2013; Salomon et al., 2016). For low Rayleigh numbers as observed here (10^{-2} - 10^{2}), depending on lens geometry), there is no convective overturning in the oil lens and heat transfer is through diffusion only. Although the timing of oil encapsulation is dependent on the oil lens thickness, thicker ice will slow down the encroaching process.

4.2.2 Stage 2: Localized upward migration in brine channels

With initial encapsulation complete, the oil/water interface remained fixed in position in growing, cold (T < -5 ˚C) sea-ice absent further large-scale oil infiltration into the ice column. At these temperatures and for sea-ice salinity of 5 g kg^{-1}, the vertical bulk permeability remains below < 10^{-11} m^2 throughout much of the ice cover, with the exception of the bottommost 10 cm. Previous experiments found that under such conditions oil is immobilized and movement confined to the 20 cm above the oil/ice interface (Dickins and DF Dickins Associates LLC, 2011; Karlsson, 2009; Martin, 1979). In our study, the extent of vertical oil penetration in brine channels at the end of the growth season was greater. In some cases, oil migrated through the full vertical depth of the ice column and surfaced within 2 days of oil release in discrete channels (Figure 6). Such oil movement has been documented in warmer ice (T>–5 °C, Karlsson et al., 2011; Martin, 1979). Nelson and Allen (1981) reported an oil-filled brine channel similar to what we observed but attributed this to an unusually thick snow cover having caused the ice to warm to close to spring temperatures, although presence of long brine channels has been observed in sea ice grown in natural environment (Cole and Shapiro, 1998).

Localized mobilization in select brine channels

Despite low ice porosity and permeability, ANS crude oil surfaced through discrete brine channels (Figure 6). This finding was unexpected: pores are typically only connected at these temperatures for porosities above 5 % (Pringle et al., 2009), and it is commonly assumed that oil is immobilized at bulk porosities below 10 % (Petrich et al., 2013). To allow oil invasion into a pore such as a brine channel, the pore needs to have an outlet for the displaced brine. Such brine displacement furthermore needs to be accommodated throughout the ice cover requiring an open and connected pore space. During the CRREL experiment, there was evidence of brine being expelled onto the top of the ice cover in the vicinity of surfacing oil. This suggests that brine is displaced as the oil invades larger, fully surface-connected channels, but further confirmation through in situ measurements (e.g., of the salinity of surfacing fluid) is needed.

Approximating the potential for oil mobilization and movement as a function of the pore size distribution and oil lens thickness holds promise (Maus et al., 2015). The Young-Laplace equation can be used to infer the minimum pore or channel diameter invaded by oil in a lens of a given thickness (Maus et al., 2013). Figure 9 suggests the oil lens thickness governs the overall penetration height within a brine channel. Initially, a thicker oil lens allows oil to move into smaller pore space. Then, hydraulic pressure drops as the oil occupies a larger vertical extent. However, once oil reaches the water level, buoyancy forces decrease as the oil lens thins. Despite the amount of oil entering the channels likely to be small compared to the oil stored in the lens, a thick oil lens counters the reduction in the driving forces (e.g. A26-20c). For thin lenses (h_{oil} <5 mm), the uptake of oil by the skeletal layer may be sufficient to prevent any further infiltration of and movement within brine channels (e.g. A28-5c).

We estimated the amount of oil stored in columnar ice brine channels to range from 0.4 to 1 Lm^{-3}. While brine tube and channel diameters vary from a few tenths of millimeters to up to 5 mm (Light et al., 2003; Petrich and Eicken, 2017), only channels with diameters greater than 1 to 2 mm have been observed to be filled with oil (Karlsson, 2009; Martin, 1979; NORCOR, 1975). We can obtain an upper bound by assuming 100 brine channels per m^2 with an idealized cylindrical geometry of 5-mm diameter extending throughout the ice cover (Lake and Lewis, 1970). Under such conditions, the oil-invadable brine channel porosity contributes at most ϕ_{bs} = 0.2 % or roughly 1/10th of the total ice porosity in winter (2 % <ϕ_{bs} <5 % for our temperature range and a salinity of 5 ‰,). Moreover, fewer than half of the brine channels were filled with oil, and oil did not always migrate through the full thickness of the ice cover in each of these. Thus, likely only half of the at most 2 Lm^{-3} oil storage capacity for fully

598 saturated brine channels (i.e, ϕ_{bs} = 0.2 %) is utilized. This is well above the minimum value of 0.04 Lm^{-3} one obtains
599 from the observation of 7 surfacing locations observed the treatment A68-90c (Figure 6) if we assume a 5-mm
600 channel diameter.

601 *Inhibition of oil movement by stratigraphic units of granular ice*

602 Granular ice stratigraphic units hinder oil movement such that oil migrating upward through channels in
603 columnar ice is stopped at the granular/columnar interface since channels do not extend past this transition in ice
604 texture (Figure 2; supplementary material Figure 14-22). Any granular ice layer, common at the surface of Arctic
605 sea-ice (Petrich and Eicken, 2017; Weeks, 2010) may thus act as a barrier to oil surfacing at least during the ice
606 growth season and the early stages of the melt season. This finding has important ramifications for oil detection
607 and spill response.

608 What is underlying cause of retardation of oil migration in granular ice? Cole and Shapiro (1998) describe
609 brine channels extending through the full thickness of a natural ice cover. However, a full-depth cross section from
610 their study indicates that the granular layer was very thin (<5 cm, Figure 3a in Cole and Shapiro, 1998), comparable
611 to quiet ice growth conditions at CRREL. Weissenberger et al. (1992) describe the pore space in granular ice as
612 a highly branched network of pores across a range of sizes. In contrast, the pore space in columnar ice is
613 characterized by straight, vertical, larger brine tubes and channels with fewer horizontal connections. Bock and
614 Eicken (2005) determined that primary – but not necessarily secondary, such as for brine channels – pore size
615 and connectivity are significantly larger in granular than in columnar ice, noting that the link between connectivity
616 and permeability is not fully understood. Lieblappen et al. (2018) conclude that columnar ice pore space has a
617 higher vertical connectivity and lower tortuosity than granular ice. With smaller grain sizes in granular ice (e.g. thin
618 section Additional material), Figure 26), larger pores located at the triple grain junctions are connected with smaller,
619 elongated pores along some of the grain boundaries forming a tortuous network.

620 Thus, any path the oil may follow through the granular layer is likely (1) to be longer than in a less tortuous
621 network - such as columnar ice - and (2) to pass through a high number of small pore spaces at grain necks/throats.
622 Consequently, the thicker the granular layer, the more difficult it is for the oil to displace the brine and invade the
623 ice volume. During the growth season, small pores closing up due to lower temperatures near the surface further
624 limit movement. As a result, the potential for oil movement through ice containing granular and columnar
625 stratigraphic units is reduced.

4.2.3 Stage 3: Mobilization with incipient bulk infiltration

During the melt season, temperature and porosity increase throughout the ice cover. The pore size distribution shifts to larger cross-sections (Bock and Eicken, 2005; Perovich and Gow, 1996) and the increase of interconnectivity leads to higher bulk permeability (Petrich and Eicken, 2017). Such changes in microstructure facilitate fluid movement through widening necks/throats and new oil or brine transport pathways are created as the expanding pores merge. As porosity increases to more than 5 to 7 %, brine movement begins in the upper ice cover (Arrigo et al., 1993; Golden et al., 2007). Pringle et al. (2007) showed that with spring warming and porosity increases pervasive brine convection, driven in part by the hydraulic head of brine suspended above the hydrostatic equilibrium level in impermeable ice resulted in overturning of brine through the full depth of the ice column. Such convective activity also likely triggers oil mobilization. As soon as porosity becomes larger than 0.05 % throughout the ice cover, the volume of oil moving into the ice increases significantly to up to 2.5 $Lm^{-2}day^{-1}$. This corresponds roughly to the bulk percolation threshold for oil used by Petrich et al. (2013). The observed daily changes in oil surfacing and migration rates (Figure 5) indicate that there is both continuous oil migration and threshold behavior. From stage II to III.

Based on ice porosity thresholds (i.e., 10%), Petrich et al. (2013) predicted oil storage capacities in the pore space near the ice–water interface up to 13 Lm^{-2} for relatively warm sea ice at Barrow, Alaska in end of May (ice thickness approx. 1.5 m). However, Maus et al. (2013) pointed out that such a porosity threshold, if it exists, should depend on the thickness of the oil lens. They concluded that the estimate of Petrich et al. (2013) may be correct for 5 to 20 mm oil lens thickness which the estimate was based on, but should be significantly higher for an oil lens thickness of, for example, 100 mm. At the end of the incipient bulk infiltration of treatment A68-90c, which started with an oil lens thickness of 90 mm, we observed that 20 Lm^{-2} of oil invaded the pore space (Figure 5). This is consistent with those earlier predictions and adds a data point to the otherwise sparse dataset available.

This uptake is equivalent to a volumetric oil content of 2.9 % by volume of ice at the end of the incipient bulk infiltration. This value falls between the oil content range of 1.2-2.6 % found by Otsuka et al. (2004) for early melt season and the value of 5.5% typically assumed for warm ice late in the melt season (Martin, 1979). Experimental conditions such as ice, $h_{ice,\,o}$, and oil lens thickness, h_o, as well as the total and normalized amount of oil in the lens, V_{oil}, have a significant effect on the total concentration of oil in the ice. We suggest that oil uptake

654 during this stage would be similar in purely columnar ice and mixed stratigraphy ice with a granular layer on top.
655 While the granular layer hinders oil transport during the growth season, the thermal evolution of the granular
656 microstructure allows brine movement soon after the onset of melt. The amount of brine pushed to the surface by
657 the oil during the CRREL experiment was not equivalent to the volume of oil (20 Lm^{-2}), indicating brine rejection at
658 the bottom as the oil moved into the pore space.

659 *Bulk infiltration in columnar ice*

660 During the early bulk infiltration phase (see Figure 5, OR+7-10 and Figure 7 OR+5/6), small volume of oil
661 moves into the ice, supporting the idea that oil is mobilized with the onset of melt (NORCOR, 1975). Results from
662 the HSVA experiment indicate that oil movement is confined to columnar ice (V_{fo} = 0.33 ± 0.27 %) with scarce
663 infiltration of the granular ice (V_{fo} = 0.06 ± 0.08%), Figure 7 OR+5/+6). Vertical sections (Additional material
664 Figure 14-22) suggest that the oil remains confined to widening vertical brine channels and feeder channels. The
665 primary pore space is likely neither connected and/or large enough. These observations are similar to the cores
666 collected after the onset of melt during the NORCOR experiment (1975, e.g. Figure 6-14 and 6-15) displaying oil-
667 filled brine channels up to the columnar/granular transition layer.

668 At OR+7, oil had invaded and surfaced through a large number of widening feeders and main brine
669 channels (Figure 24). With a channel density of 170 m^{-2} and 5-mm diameter, the estimated oil intake into the brine
670 channels of 0.67 Lm^{-2} converts to an average oil concentration of 0.4 vol-% in columnar ice (excluding the skeletal
671 layer). This value is on the lower side of the oil concentration measured directly on the ice sample (V_{fo} = 0.7 ± 0.5
672 vol-%, Figure 7a). As most of the ice matrix in columnar ice remains unoiled, we estimated that amount of oil
673 moving occupying the feeder channels account for half of the amount of oil moving into the brine channels.

674 *Bulk infiltration in granular ice*

675 In granular ice, the heterogeneity of the oil migration visible in Figure 7b is associated with two distinct
676 modes of oil infiltration. First, despite increased permeability, the granular microstructure remains impermeable to
677 oil movement, leading to an absence or low amounts of oil (V_{fo} <= 0.2 %). Second, oil is able to migrate through
678 the granular microstructure with pronounced fanning or branching of infiltration pathways indicating a lack of less
679 tortuous paths that are wider. Oil invades a larger fraction of the open, accessible pore space as it finds a pathway
680 to the surface, resulting in both a large amount of oil moving into the granular layer in the oil volume fraction (V_{fo}
681 = 4.8 ± 1.6 %) if oil reached the surface, or limited in samples exempt of oil surfacing (V_{fo} = 0.1 ± 0.1 %). Although

682 the lack of characterization of granular ice limits our understanding, we explained the large variability by the
683 presence or the absence of a preferential pathway that allows for brine and oil displacement (Figure 23). At the
684 end of incipient bulk infiltration, the combination of these two infiltration modes results in a random distribution of
685 oil surfacing locations (Supplemental material: Figure 25).

686 ### 4.2.4 Stage 4: Steady state infiltration with asymptotic saturation of the pore
687 space

688 In later stages of ice melt, the distinction between brine pores, layers and channels is difficult due to the
689 highly interconnected nature of the pore space and the overall increase in pore volume (Petrich and Eicken, 2017).
690 While increased permeability enhances oil mobility compared to stage 3, we observed a decrease in oil flow rate,
691 likely linked to pore space increasingly saturated with oil, or shifts in the force balance between oil present at the
692 surface and remaining in the lens.

693 While surface and mid-depth temperature do not change much between OR+17 and OR+27 (Figure 5),
694 small changes in temperature have strong effects on brine-filled microstructure at such high temperatures. In
695 addition, the saturation is increasing during this stage, as expected as more oil migrates upward. We observed
696 major spreading and even pooling of oil at the surface with the warming of the ice. Estimating the amount of oil at
697 the surface is difficult, as even a little oil blackens the ice fully. At OR+27, 20 Lm^{-2} of oil remain in the oil lens, while
698 roughly 30 Lm^{-2} moved into the ice, corresponding to an average oil content of 4.4 vol-% across the entire ice
699 thickness, close to the measured 5.1 vol-% for the NORCOR (1975) experiments with comparable oil density.

700 As oil moves through the ice, buoyancy forces driving upward oil migration decrease proportionally to the
701 height of oil above the water (Figure 11). The resulting force balance for vertical oil movement makes it harder for
702 oil to move upward, hence the vertical oil flow decreases. With an average difference density of 100 kg m^{-3} between
703 oil and sea water, the maximum oil thickness pooling at the ice surface would be approximatively 10% of the
704 original oil lens volume. However, horizontal spreading within the pore space near the freeboard level or at the ice
705 surface increases the potential for the total volume of oil migrating to the surface (Figure 11).

4.2.5 Stage 5: Disintegration of the sea-ice cover

Towards the end of the melt period, increasing air temperature (OR+27) led to faster ice melt. At the surface, temperature may exceed the freezing point of sea water as the ice is fully desalinated (Figure 5). Accumulation of oil in the uppermost ice layer and oil pooling at the surface led to preferential heating of the oiled ice (Pegau et al., 2016). Therefore, oiled ice melts faster and pooling in such locations increases. Observations made on melting ice at UAF and CRREL after the end of the experiment indicate that rotten ice floes filled with oil are surrounded by oil-covered water.

4.3 Impact of oil properties

The striking differences of oil penetration into columnar cold ice between ANS and Troll B oil (Figure 9) are likely linked to intrinsic oil properties such as pour point and viscosity. Generally speaking, oil migrates upwards if buoyancy forces overcome the hydraulic head, capillary and interfacial forces, the latter depending strongly on pore diameter, surface tension and pour point.

Initially, capillary forces dictate the potential for oil to invade a pore space of a given diameter occupied by brine (Maus et al., 2013). As the oil moves within the pore, new contact surface between oil and ice is created proportionally to the penetration depth. Once the connected pore space is filled with oil, oil viscosity is important to estimate the timing of the migration. ANS crude oil penetrated deeper into the ice (up to the full ice thickness) than Troll B oil, which stopped roughly halfway, even though buoyancy would have been greater during the Troll B treatments (B20-30c) due to lower density oil and thicker oil lenses. This suggests that despite being the essential driving force pushing the oil to the surface, the oil density plays a minor role for overall flow behavior compared to other oil properties that can decrease capillary forces.

As per the data sheets, viscosity at 20 °C and pour point are similar for both oil types (Table 2), yet we observed different flow behavior: while the ANS crude oil flowed freely at -40 °C, Troll B oil did flow during oil injection at –10 °C but did not flow during sample processing at -15 °C. Even disregarding the possibility of differences between individual batches, the expected reproducibility of pour point measurements is less than 6°C (e.g., ASTM International, 2005), which is not sufficient to make predictions about oil movement at temperatures near the stated pour point. In addition, as oil are re-homogenized prior to measurement in laboratory, their

properties, may not be representative of oil spills in cold environments, as well as during an experiment, that could have experienced shear during transportation or stratification during storage. Ultimately the pour point serves as a threshold measure that describes the potential of oil to flow at a given temperature. At temperatures below the pour point, oil remains immobile.

5 Conclusion

Through the combined interpretation of three separate experiments we have identified five distinct stages of upward oil migration throughout a full seasonal cycle (Figure 11, Table 4). In the first stage, oil quickly saturates the open and highly connected skeletal layer. In the second stage, oil is immobilized as effective bulk permeability remains low until the end of the growth season. However, small quantities of oil are able to migrate upward in discrete, large channels. In the third stage, at the onset of melt, oil becomes mobilized when permeability increases above approximately 10^{-11} m^2. Up to 20 Lm^{-2} of oil is entrained into 60-cm thick ice in 6 days, equivalent to 3% oil volume fraction in the ice. As much as 1/3 of the bulk porosity is infiltrated by oil. In the fourth stage, slow warming of the ice leads to asymptotic behavior as the bulk porosity increases slowly and oil invades much of the pristine primary and secondary pore space. Finally, rapid warming of air temperature prior to complete ice melt leads to a rotten ice microstructure(Frantz et al., 2019), in which oil invades most of the inter- and intragranular pore space. Up to 40 Lm^{-2} is entrained in a 60-cm thick ice cover, equivalent to 6 % oil volume fraction in the ice.

While our analysis is consistent with previous findings - encapsulated oil during the growth season is mobilized in spring (Karlsson et al., 2011; Martin, 1979; NORCOR, 1975) –, we highlight two different mechanisms in oil migration throughout the seasonal cycle. In warm ice (T > -5 °C), the higher and more interconnected porosity facilitates brine and oil displacement and bulk properties of the ice, such as permeability, govern the oil movement (Maus et al., 2015; Petrich et al., 2013). In colder ice, oil migration requires the existence of a pathway connecting the oil lens to the surface, and is constrained by the existence of necks/throats along this pathway that may constrict the flow. Additionally, we highlight the role of sea-ice textural units in impeding the surfacing of oil, in particular in cold ice. Our analysis suggests that the more tortuous pore space of granular ice hinders oil movement, while the presence of large vertical pore features in columnar ice facilitates upward oil migration. With the predicted increase of open water in the Arctic ocean, the ratio of granular to columnar ice is also likely to

increase. Further work is required to quantify the impact of the microstructural differences of granular and columnar ice on oil transport processes through sea-ice.

Both oil lens thickness and oil volume have a noticeable impact on upward oil migration. Natural spreading of the oil underneath the level ice leads to an equilibrium thickness ranging from 1 to 2 cm (Keevil and Ramseier, 1975; Kovacs et al., 1981) - more than the minimal oil lens thickness (h_{oil}> 5mm) required for oil penetration into the skeletal layer as per our observations. Ice bottom roughness allows oil pooling in cavities up to 9 cm deep (Dickins et al, 2011), thus providing enough buoyancy for the oil to be also migrate deeper into the ice matrix. In stage II and early in stage III, the vertical extent of oil in the brine channels governs the oil flow, as the hydrostatic oil pressure increases with the oil penetration depth. Later (late stage III, stages IV, V), the thickness is an important factor, as a large reservoir is required to maintain a sufficient buoyancy (V> 20 Lm^{-2} of oil for 0.7 m thick ice) to keep oil moving upwards., once oil reaches the water level. In addition, viscous properties of the oil determine its ability to flow at low temperatures.

The potential for oil movement within the brine channels in cold ice has important environmental impacts. Despite the limited volume of oil, a larger volume of ice than previously thought may be affected in the event of an oil spill during the growth season, as oil moved through the full extent of columnar ice, rather than being confined to the lower 20 to 30 cm. Our findings improve understanding of oil movement through the full depth of the sea-ice cover during a complete simulated seasonal cycle and may in the future contribute to the development of a predictive oil migration model, which will provide timing on oil movement and oil distribution in support of operational spill response and assessment (Alaska Clean Seas, 2017). In a broader context, integrating an oil distribution model with a large-scale oil spill trajectory forecasting model will be a crucial improvement in emergency planning and will support the quantification of harm to ice-associated biological communities and ecosystems in the aftermath of any spills, as well as benefit natural resource damage assessments (NRDA) and net environmental benefit analyses (Bejarano et al., 2014).

6 Acknowledgements

The experiment and analysis of data at CRREL and UAF were supported by the Oil Spill Recovery Institute, Cordova, Alaska with a funding provided by a Joint Industry Program on Remote Sensing of Oil in Ice (14-50-01), and a Graduate Research Fellowships (16-10-08). The experiment and analysis at UAF were

supported by the Bureau of Ocean Energy Management, Alaska via a grant of the Coastal Marine Institute (M14AC0001). The helpful attitude of technicians at HSVA and CRREL is gratefully acknowledged and contributed to the success of both projects. Special thanks to Kyle Dilliplaine, and the researcher team involved in the Remote Sensing of Oil-in-Ice experiments at CRREL. ANS crude oil was provided by Alyeska Pipeline Company and Troll B Crude oil by Equinor (previously Statoil). The experiments and analysis of data at HSVA were financed by the Research Council of Norway through grants 243812 (PETROMAKS2 project MOSIDEO) and 237906 (SFI CIRFA). The comment of two anonymous reviewers improved this paper.

7 Bibliography

Alaska Clean Seas, 2017. Alaska Clean Seas Technical Manual, Volume 1, Tactics Descriptions. 191 pp.

AMAP, 2007. Arctic Oil and Gas 2007. Arctic Monitoring and Assessment Programme (AMAP) Oslo, Norway. 40 pp.

Arctic Council, 2013. Agreement on Cooperation on Marine Oil Pollution Preparedness and Response in the Arctic. Arctic Council Secretariat. Tromsø, Norway.

Arrigo, K. R., Kremer, J. N., & Sullivan, C. W. 1993. A simulated Antarctic ast ice ecosystem. Journal of Geophysical Research: Oceans, 98(C4), 6929–6946. https://doi.org/10.1029/93jc00141

ASTM International, 2005. ASTM Standard D97-05. Stand. Test Method Pour Point Pet. Prod. https://doi.org/10.1520/D0097-17A

Barnhart, K.R., Miller, C.R., Overeem, I., Kay, J.E., 2015. Mapping the future expansion of Arctic open water. Nat. Clim. Chang. 6, pp. 1–6. https://doi.org/10.1038/nclimate2848

Bauer, J., Martin, S., 1983. A model of grease ice growth in small leads. J. Geophys. Res. 88, 2917–2925. https://doi.org/10.1029/JC088iC05p02917

Bejarano, A.C., Michel, J., Allan, S.E., 2014. Guidelines for Collecting High Priority Ephemeral Data for Oil Spills in the Arctic in Support of Natural Resource Damage Assessments. National Oceanic and Atmospheric Administration. Office of Respone and Restoration. Anchorage. 284 pp.

Bock, C., Eicken, H., 2005. A magnetic resonance study of temperature-dependent microstructural evolution and self-diffusion of water in Arctic first-year sea ice. Ann. Glaciol. 40, pp 179–184. https://doi.org/10.3189/172756405781813645

Buist, I.A., Dickins, D.F., 1983. Fate and Behaviour of Water-in-Oil Emulsions in Ice. Proc. Arct. Mar. OIl Spill Program. Tech. Semin. Edmonton, Alberta. June 14-16. pp.263-279.

Cole, D.M., Shapiro, L.H., 1998. Observations of brine drainage networks and microstructure of first-year sea ice. J. Geophys. Res. 103, pp. 21739–21750. https://doi.org/10.1029/98JC01264

Collins, R.E., Bluhm, B., Gradinger, R., Eicken, H., Oggier, M., Dilliplaine, K.B., 2017. Crude oil infiltration and movement in first-year sea ice : Impacts on ice-associated biota and physical constraints. Coastal Marine Institute Final Project Report, Fairbanks. 72 pp.

Cox, G.F.N., Weeks, W.F., 1983. Equations for determining the gas and brine volumes in sea - ice samples. J. Glaciol. 29, pp.306–316.

Dickins, D., DF Dickins Associates LLC, 2011. Behavior of Oil Spills in Ice and Implications for Arctic Spill Response, In Proceedings of the OTC Arctic Technology Conference. Houston, Texas. February 7-9. 15 pp.

Dickins, D., DF Dickins Associates LLC, 1992. Behavior of Oil Spilled at Sea (BOSS): Oil-in-Ice Fate and Behaviour. Report prepared for Environment Canada, U.S. Minerals Management Service, and American Petroleum Institute 342 pp.

Dickins, D., Liberty, L., Hirst, W., Bradford, D., Jones, V., Zabilansky, L., Gibson, G., Lane, J., 2005, New and Innovative Equipment and Technologies for the Remote Sensing and Surveillance of Oil in and Under Ice. Report prepared for U.S. Minerals Management Service, 170 pp.

Eguíluz, V.M., Fernández-Gracia, J., Irigoien, X., Duarte, C.M., 2016. A quantitative assessment of Arctic shipping in 2010–2014. Sci. Rep. 6, 30682. https://doi.org/10.1038/srep30682

Eicken, H., 2016. Automated ice mass balance site (SIZONET). Arctic Data Center doi:10.18739/A2D08X

Eicken, H., B.A. Bluhm, R.E. Collins, R.R. Gradinger, C. Haas, M. Ingham, A. Mahoney, M. Nicolaus, D. Perovich (2014) “Field Techniques in Sea- Ice Research” in Cold Regions Science and Marine Technol- ogy, [Ed. H. Shen], in Encyclopedia of Life Support Systems (EOLSS), Developed under the Auspices of the UNESCO, Eolss Publishers, Paris, France, [http://www.eolss.net]

Fingas, M.F., Hollebone, B.P., 2003. Review of behaviour of oil in freezing environments. Mar. Pollut. Bull. 47, pp. 333–340. https://doi.org/10.1016/S0025-326X(03)00210-8

Frantz, C.M., Light, B., Farley, S.M., Carpenter, S., Lieblappen, R., Courville, Z., Orellana, M. V., Junge, K., 2019. Physical and optical characteristics of heavily melted “rotten” Arctic sea ice. Cryosph. 13, pp. 775–793. https://doi.org/10.5194/tc-2018-141

Freitag, J., 1999. The hydraulic properties of Arctic Sea-Ice - Implications for the small scale particle transport. Ph.D. Thesis, Alfred-Wegener-Institut fur Polar- und Meeresforschung. 325 pp.

Galley, R.J., Else, B.G.T., Geilfus, N., Hare, A.A., Isleifson, D., Barber, D.G., Rysgaard, S., 2015. Imaged brine inclusions in young sea ice — Shape , distribution and formation timing. Cold Reg. Sci. Technol. 111, pp. 39–48. https://doi.org/10.1016/j.coldregions.2014.12.011

Glaeser, J.L., Vance, G.P., 1972. A Study of the Behavior of Oil Spills in the Arctic, In Proceedings of the Offshore Technology Conference. Houston, Texas. May 1-3, 14 pp.

Golden, K.M., Eicken, H., Heaton, a. L., Miner, J., Pringle, D.J., Zhu, J., 2007. Thermal evolution of permeability and microstructure in sea ice. Geophys. Res. Lett. 34, pp. 1–6. https://doi.org/10.1029/2007GL030447

Gough, A.J., Mahoney, A.R., Langhorne, P.J., Williams, M.J.M., Haskell, T.G., 2012. Sea ice salinity and structure: A winter time series of salinity and its distribution. J. Geophys. Res. Ocean. 117, pp. 1–12. https://doi.org/10.1029/2011JC007527

Hilcorp Alaska LLC, 2015, Liberty Project. Retrieved July 28, 2019, from Bureau of Ocean energy Management website: https://www.boem.gov/Hilcorp-Liberty/

Karlsson, J., 2009. A laboratory study of fixation, release rates and small scale movement of oil in artificial sea ice. MSc Thesis, University of Copenhagen. 199 pp.

Karlsson, J., Petrich, C., Eicken, H., 2011. Oil Entrainment and Migration in Laboratory-grown Saltwater Ice. Proc. 21st Int. Conf. Port Ocean Eng. under Arct. Cond (POAC). pp 1–10.

Keevil, B.E., Ramseier, R.O., 1975. Behavior of Oil Spilled Under Floating Ice. Int. Oil Spill Conf. Proc. 1975, pp. 497–501. https://doi.org/10.7901/2169-3358-1975-1-497

Kovacs, A., Morey, R.M., Cundy, D.F., Decoff, G., 1981. Pooling of oil under sea ice, in: Port and Ocean Engineering Under Arctic Conditions. Quebec City, pp. 912–922.

Lake, R.A., Lewis, E.L., 1970. Salt rejection by sea ice during growth. J. Geophys. Res. 75, pp. 583–597. https://doi.org/10.1029/JC075i003p00583

Leppäranta, M., Manninen, T., 1988. The brine and gas content of sea ice with attention to low salinities and high temperatures. Helsinki, Finland, Finnish Institute of Marine Research, Finnish Institute of Marine Research Internal Report. 15 pp.

Lieblappen, R.M., Kumar, D.D., Pauls, S.D., Obbard, R.W., 2018. A network model for characterizing brine channels in sea ice. The Cryosphere, 12, pp.1013–1026. https://doi.org/10.5194/tc-12-1013-2018

Light, B., Maykut, G.A., Grenfell, T.C., 2003. Effects of temperature on the microstructure of first-year Arctic sea ice. J. Geophys. Res. Ocean. 108. https://doi.org/10.1029/2001JC000887

Markus, T., Stroeve, J.C., Miller, J., 2009. Recent changes in Arctic sea ice melt onset, freezeup, and melt season length. J. Geophys. Res. Ocean. 114, pp. 1–14. https://doi.org/10.1029/2009JC005436

Martin, S., 1979. A field study of brine drainage and oil entrainment in first-year sea ice. Deep Sea Res. Part B. Oceanogr. Lit. Rev. 22, pp. 473–502. https://doi.org/10.1016/0198-0254(80)95767-2

Maus, S., Becker, J., Leisinger, S., Matzl, M., Schneebeli, M., Wiegmann, A., 2015. Oil saturation of the sea ice pore space. Proc. 23st Int. Conf. Port Ocean Eng. under Arct. Cond. pp. 1–12.

Maus, S., Leisinger, S., Matzl, M., Schneebeli, M., Wiegmann, A., 2013. Modelling oil entrapment in sea ice on the basis of 3d micro-tomographic images. Proc. 22st Int. Conf. Port Ocean Eng. under Arct. Cond (POAC). pp 1–10.

Nelson, W.G., Allen, A.A.A., 1981. Oil Migration and Modification Processes in Solid Sea Ice. Int. Oil Spill Conf. Am. Pet. Inst. 1, pp. 191–198.

NORCOR, 1975. The Interaction of Crude Oil With Arctic Sea Ice, Canadian D. ed, Beaufort Sea Project Technical Report No. 27. Victoria, BC, Canada. 213 pp.

O'Sadnick, M., Petrich, C., Phuong, N.D., 2017. The entrainment and migration of crude oil in sea ice, the use of vegetable oil as a substitute, and other lesson from laboratory experiments. Proc. 24th Int. Conf. Port Ocean Eng. Under Arct. Cond. (POAC), Busan, Korea, 12 pp.

Otsuka, N., Kondo, H., Saeki, H., 2004. Experimental study on the characteristics of oil ice sandwich. Ocean. '04 MTS/IEEE Techno-Ocean '04 (IEEE Cat. No.04CH37600) 3, 1470–1475. https://doi.org/10.1109/OCEANS.2004.1406337

Pegau, W.S., Garron, J., Zabilansky, L., Bassett, C., Bello, J., Bradford, J., Carbns, R., Courville, Z.R., Eicken, H., Elder, B., Eriksen, P., Lavery, A., Light, B., Maksym, T., Marshall, H.-P., Oggier, M., Perovich, D.K., Pacwiardowski, P., Singh, H., Tang, D., Wiggins, C., Wilkinson, J.P., 2016. Detection of oil on-in-and-under ice - Final Report 5.3, Arctic Response Technology, http://www.arcticresponsetechnology.org/wp-content/uploads/2013/10/Report 5.1 - SURFACE REMOTE SENSING.pdf

Perovich, D.K., Gow, A.J., 1996. A quantitative description of sea ice inclusions. 1996. Journal of Geophysical Research: Oceans, 101(C8), https://doi.org/10.1029/96JC01688

Petrich, C., Arnsten, M., 2013. Laboratory Studies of Oil Encapsulation Under, in: Proc. of the 22st International Conference on Port and Ocean Engineering under Arctic Conditions (POAC). pp. 1–10.

Petrich, C., Eicken, H., 2017. Overview of sea ice growth and properties, in: Thomas, D.N. (Ed.), Sea Ice. John Wiley & Sons, Ltd, pp. 1–41. https://doi.org/10.1002/9781118778371.ch1

Petrich, C., Karlsson, J., Eicken, H., 2013. Porosity of growing sea ice and potential for oil entrainment. Cold Reg. Sci. Technol. 87, pp. 27–32. https://doi.org/10.1016/j.coldregions.2012.12.002

Petrich, C., O'Sadnick, M., Brekke, C., Myrnes, M., Maus, S., Salomon, M.L., Woelk, S., Grydeland, T., Jenssen, R.O., Eicken, H., Oggier, M., Ferro-Famil, L., Harkati, L., Ott, R., Reimer, N., 2018. An Overview of the

MOSIDEO/CIRFA Experiments on Behavior and Detection of Oil in Ice. In Proceedings of the 41st AMOP technical seminar on environmental contamination and response, Victoria, BC, pp. 112–122.

Pringle, Daniel J., Dubuis, G., Eicken, H., 2009. Instruments and Methods Impedance measurements of the complex dielectric permittivity of sea ice at 50 MHz : pore microstructure and potential for salinity monitoring. J. Glaciol. 55, pp. 81–94.

Pringle, D.J., Eicken, H., Trodahl, H.J., Backstrom, L.G.E., 2007. Thermal conductivity of landfast Antarctic and Arctic sea ice. J. Geophys. Res. 112, C04017. https://doi.org/10.1029/2006JC003641

Pringle, D. J., Miner, J.E., Eicken, H., Golden, K.M., 2009. Pore space percolation in sea ice single crystals. J. Geophys. Res. 114, C12017. https://doi.org/10.1029/2008JC005145

Salomon, M.L., Maus, S., Arntsen, M., O'Sadnick, M., Petrich, C., Wilde, F., 2016. Distribution of oil in sea ice : Laboratory Experiments for 3-dimensional microCT investigations. Proc. Twenty-sixth Int. Ocean Polar Eng. Conf. 880653.

Smith, L.C., Stephenson, S.R., 2013. New Trans-Arctic shipping routes navigable by midcentury. Proc. Natl. Acad. Sci. U. S. A. 110, E1191-5. https://doi.org/10.1073/pnas.1214212110

Statoil (2011), Troll Blend Crude Oil Assay, Crude Summary Report Reference TROLLBLEND201101, Statoil, Stavanger, Norway, 1 pp.Weeks, W.F., 2010. On sea ice. University of Alaska Press, Fairbanks.

Weissenberger, J., Dieckmann, G., Gradinger, R., Spindler, M., 1992. Sea ice: A cast technique to examine and analyze brine pockets and channel structure. Limnol. Oceanogr. 37, pp. 179–183. https://doi.org/10.4319/lo.1992.37.1.0179

Wells, A.J., Wettlaufer, J.S., Orszag, S.A., 2011. Brine fluxes from growing sea ice 38, pp. 1–5. https://doi.org/10.1029/2010GL046288

Wilkinson, J.P., Beegle-Krause, C., Evers, K.U., Hughes, N., Lewis, A., Reed, M., Wadhams, P., 2017. Oil spill response capabilities and technologies for ice-covered Arctic marine waters: A review of recent developments and established practices. Ambio 46, pp. 423–441. https://doi.org/10.1007/s13280-017-0958-y

930 Wilkinson, J.P., Wadhams, P., Hughes, N.E., 2007. Modelling the spread of oil under fast sea ice using three-
931 dimensional multibeam sonar data. Geophys. Res. Lett. 34, L22506. https://doi.org/10.1029/2007GL031754

932 Wolfe, L.S., Hoult, D.P., 1974. Effets of oil under sea ice. J. Glaciol. 13, pp. 473–488.

933 Zubov, N.N., 1963. Arctic Ice. U.S. Naval Electronics Laboratory, San Diego, California. 510 pp.

934 8 Additional material

935 8.1 CRREL experiment

Figure 12 – Oil pooling at the surface of A54-60c at OR+34 at CRREL

936

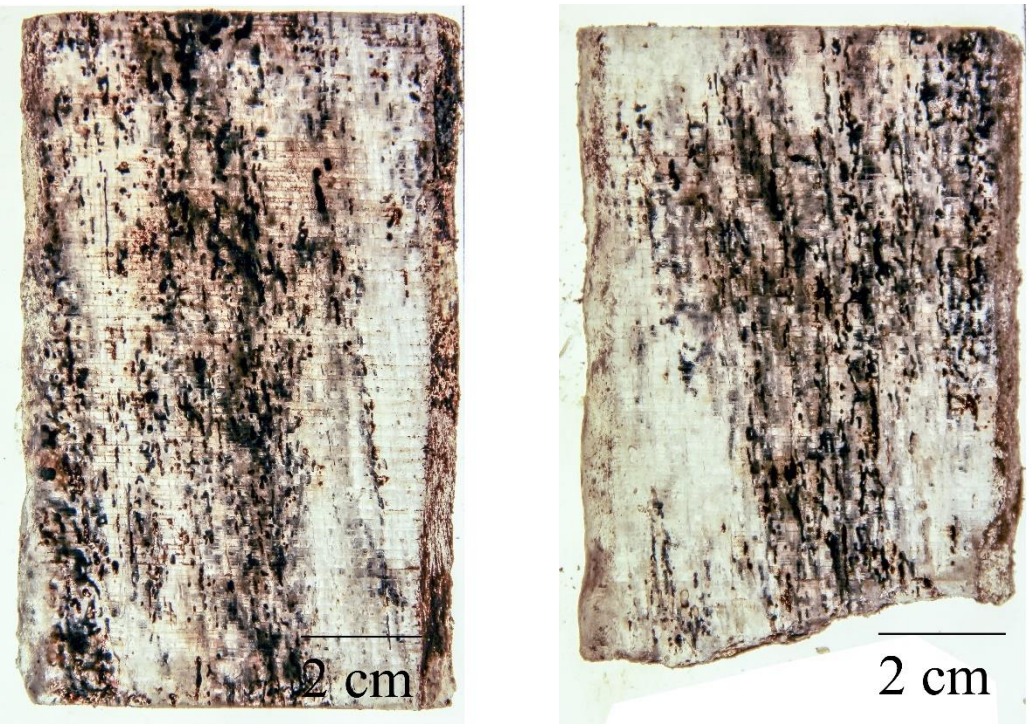

Figure 13 – Vertical thick section at depth (a) 11-22 cm and (b) 22-32 cm at OR+34 for A54-60-c at CRREL. Note how the oil invaded both inter- and intragranular pore space.

8.2 HSVA evolution

Figure 14 – Vertical section in columnar stratigraphy at OR+3 at HSVA

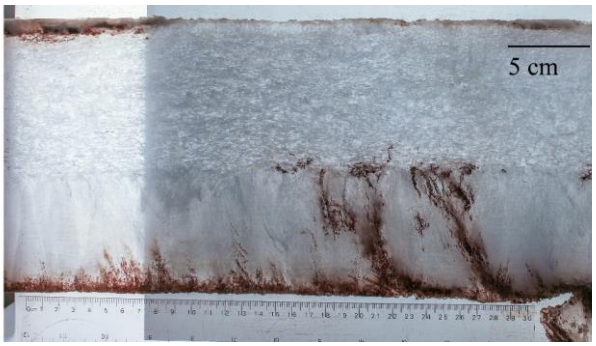

Figure 15 – Vertical section in mixed stratigraphy at OR+3 at HSVA

Figure 16 – Vertical section in columnar stratigraphy at OR+4 at HSVA

Figure 17 – Vertical section in mixed stratigraphy at OR+4 at HSVA

Figure 18 – Vertical section in columnar stratigraphy at OR+5 at HSVA

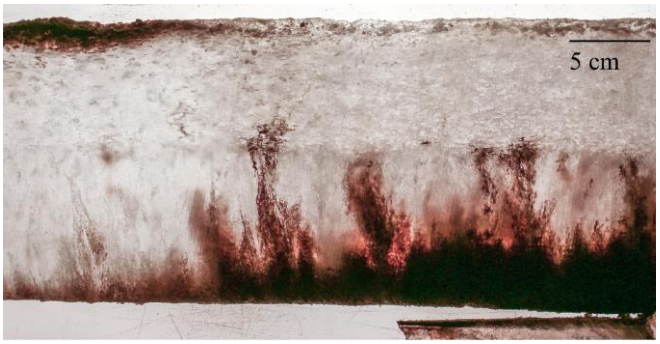

Figure 19 – Vertical section in mixed stratigraphy at OR+5 at HSVA

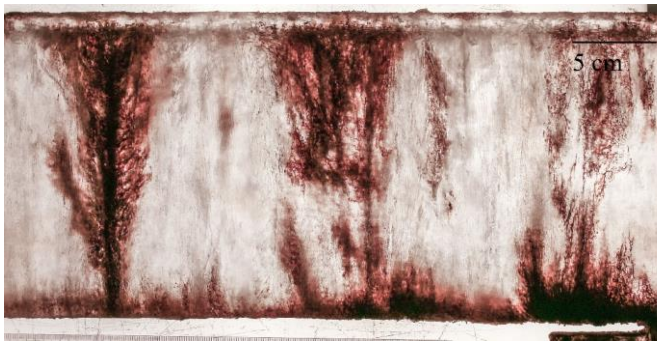

Figure 20 – Vertical section in columnar stratigraphy at OR+6 at HSVA

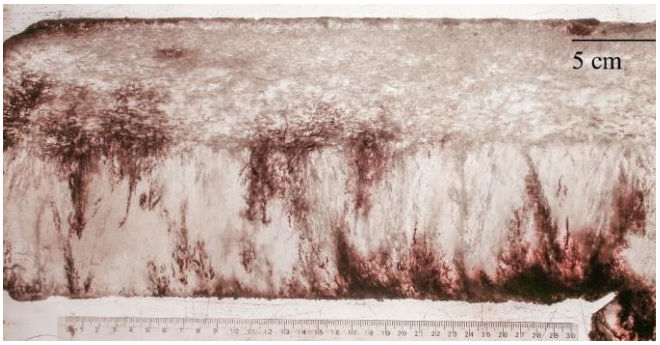

Figure 21 – Vertical section in mixed stratigraphy at OR+6 at HSVA

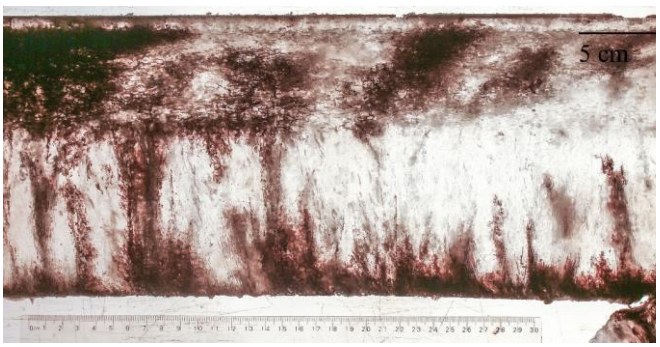

Figure 22 – Vertical section in columnar stratigraphy at OR+7 at HSVA

Figure 23 – Vertical section in mixed stratigraphy at OR+7 at HSVA

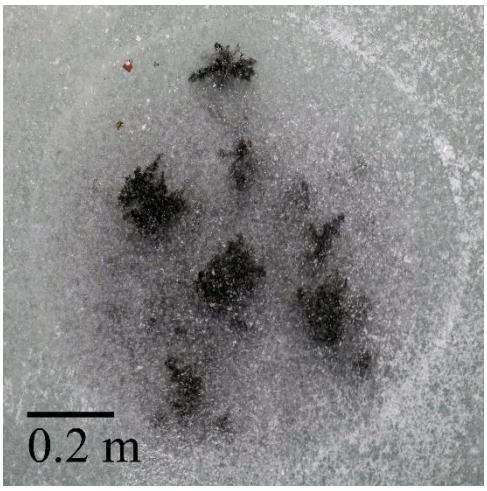

Figure 24 – Ice surface in columnar ice at OR+7 at HSVA

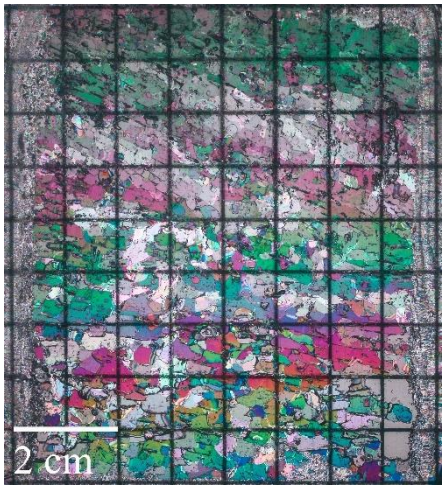

Figure 25 – Ice surface in mixed ice at OR+7 at HSVA

Figure 26 – Vertical thin cross section of granular sea ice in mixed ice stratigraphy at HSVA at OR+0

Figure 27 – Vertical thin cross section of transition granular to columnar sea ice in mixed ice stratigraphy at HSVA at OR+0